A glacial chronology for sub-Antarctic Marion Island from MIS 2 and MIS 3

Elizabeth M. Rudolph [a,*], David W. Hedding [b], Dominic A. Hodgson [c], Derek Fabel [d], Delia M. Gheorghiu [d], Richard Shanks [d], Werner Nel [e]

[a] Afromontane Research Unit, Department of Geography, University of the Free State, Bloemfontein, South Africa
[b] Department of Geography, University of South Africa, Pioneer Avenue, Florida, 1710, South Africa
[c] British Antarctic Survey, High Cross, Madingley Road, Cambridge, CB3 0ET, United Kingdom
[d] Scottish Universities Environmental Research Centre, Rankine Avenue, East Kilbride, G75 0QF, United Kingdom
[e] Department of Geography and Environmental Science, University of Fort Hare, 1 King Williamstown Road, Alice, 5700, South Africa

A B S T R A C T

It is increasingly apparent that local and regional factors, including geographic location, topography and climatic variability, strongly influence the timing and extent of glaciations across the Southern Hemisphere. Glacial chronologies of sub-Antarctic islands can provide valuable insights into the nature of regional climatic variability and the localised response(s) of glacial systems during periods of climatic change. With new cosmogenic ^{36}Cl exposure ages from Marion Island in the southern Indian Ocean, we provide the oldest dated terrestrial moraine sequences for the sub-Antarctic islands. Results confirm that a local Last Glacial Maximum was reached prior to ~56 ka when ice retreated with localised stand still events at ~43 ka and between ~38 and 33 ka. Evidence of ice re-advances throughout MIS 2 are limited and particularly absent for the cooling periods at ~32 and ~21 ka, and retreat continued until ~17 ka ago. Any MIS 1 readvances on the island would be confined to altitudes above 900 m a.s.l. but the Holocene exposure ages remains to be documented. We compare Marion Island's glacial chronology with other sub-Antarctic islands (e.g., the Kerguelen archipelago, Auckland and Campbell islands and South Georgia) and review the evidence for a Southern Hemisphere glacial maximum in late MIS 3 (~41 ka). At a regional scale we recognize sea surface temperatures, sea ice extent and the latitudinal position of the Southern Westerly Wind belt as key controls on equilibrium-line altitudes and ice accumulation due to their influence on air temperature and precipitation regimes. At an island scale, geomorphological mapping shows that deglaciation of individual glacier lobes was a-synchronous due to local physiographical and topographical factors controlling the island's micro-climate. We suggest that variability in deglaciation chronologies at smaller scales (particularly at the sub-Antarctic Islands) are important to consider when untangling climatic drivers across the Southern Ocean.

1. Introduction

Southern Hemisphere glacial chronologies provide us with valuable insights into the spatiotemporal variability of regional climatic drivers (Knight et al., 2021). Over the last decade, the application of a suite of palaeo-climatic proxies and geochronological dating methods have allowed significant progress to be made in reconstructing regional glacial oscillations throughout the Quaternary (e.g., Darvill et al., 2016; Hodgson et al., 2014b; Petherick et al., 2022; Shulmeister et al., 2019). Across the sub-Antarctic, the spatio-temporal patterns of maximum ice extent and deglaciation are relatively well constrained for Marine oxygen Isotope Stage 2 (MIS 2) (e.g. Darvill et al., 2016; Hodgson et al.,

2014a; Jomelli et al., 2017; Rudolph et al., 2020; Shulmeister et al., 2019; White et al., 2018) and MIS 1 and the late Holocene (e.g. Charton et al., 2022; Graham et al., 2017; Köse et al., 2022; Solomina et al., 2016, 2015; Verfaillie et al., 2021). The geographical variability of deglaciation patterns at the islands has generally been attributed to a number of factors, including the migration of ocean fronts and/or Southern Westerly Wind belt (see De Boer et al., 2013; Denton et al., 2021; Doughty et al., 2015; Petherick et al., 2022; Putnam et al., 2013; Schaefer et al., 2015; Sime et al., 2013) and their impact on precipitation regimes. Unlike the continental ice masses and larger mountain glaciers of the Southern Hemisphere (e.g., Antarctica, the Andes, the Southern Alps), the sub-Antarctic islands (e.g. Kerguelen Archipelago, Marion Island,

South Georgia, Heard Island etc.) are more sensitive to variations in regional scale climatic drivers due their small sub-aerial size, generally lower altitude and hyper-maritime climate. In addition, these islands provide the only terrestrial records of climate change across the vast Southern Ocean (Hodgson et al., 2014b) and, therefore, are vital for understanding trends and variability of regional-scale climatic drivers. Despite the recent progress, much remains unknown about the glacial oscillations of the sub-Antarctic throughout MIS 3 (time-slice ~36–57 ka ago; Railsback et al., 2015).

At sub-Antarctic Marion Island, initial cosmogenic ^{36}Cl exposure ages provide a glacial record for MIS 2, showing that deglaciation commenced prior to 34 thousand years (34 ka) ago and continued until ~17 ka ago (Rudolph et al., 2020). This chronology was reconstructed from a single altitudinal transect on the north-eastern slopes of the island leaving uncertainty about the timing of the local Last Glacial Maximum and the pattern of subsequent island-scale deglaciation. The limited spatial distribution of glaciated surfaces across Marion Island, mostly due to over printing by post-glacial volcanism, have posed several challenges to a holistic glacial reconstruction for the island. Nevertheless, a recent, comprehensive record of the island's glacial geomorphology (Rudolph et al., 2021a) has supported a revised spatial reconstruction of the island's palaeo-ice extent and glacial basins (Rudolph et al., 2022a). This spatial data allowed for a more targeted sampling strategy for further ^{36}Cl exposure dating, which we present in this paper, expanding the chronological record to the western, southern, and northern sectors of Marion Island. In this paper we provide thirty-three new ^{36}Cl surface exposure ages from fifteen sites including moraines, glaciated bedrock and a dilatation outcrop (which may be attributed to glacial unloading; Rudolph et al., 2021a).

2. Study area & methods

2.1. Geographical setting

Sub-Antarctic Marion Island (46°54′S, 37°45′E) is a volcanic island with a sub-aerial extent of 293 km^2 and a maximum elevation of 1240 m a.s.l. (Fig. 1). The island's ~1 million year old volcanic history is dominated by basaltic effusions and brief explosive events which gave rise to a substrate of predominantly alkali basalts (Le Roex et al., 2012; McDougall et al., 2001). The surface geology is colloquially referred to as pre-glacial 'grey' lavas and post-glacial 'black' lavas, referring to surfaces that pre- and post-date an extensive glacial period (Verwoerd, 1971) (Fig. 1 C). The island is currently ice-free, save for debris-covered ice in the Central Highland (at altitudes above 1000 m a.s.l.) (Hedding, 2008). Studies on landscape evolution have included proxies on the rates of weathering (Sumner et al., 2002), periglacial processes (Boelhouwers et al., 2003), soil and peat formation (Haussmann et al., 2010) and ecological succession (Chau et al., 2019). The geochemical characteristics of the island substrate limit the application of geochronological dating techniques to cosmogenic ^{36}Cl exposure dating (Nel et al., 2021).

The island currently receives ~2000 mm annual rainfall and has a mean annual air temperature of between 5 and 6 °C (Hedding and Greve, 2018; Nel et al., 2023). The geographic location and hyper-maritime setting of Marion Island results in an island climate largely controlled by the Southern Westerly Wind belt and sea-surface temperatures, i.e., the position of oceanic fronts (Fig. 1 B). However, Toolsee & Lamont (2022) recently determined that the high variability of the island's long-term climate is weakly correlated to the Southern Annular Mode and the El Niño Southern Oscillation. Despite records showing a steady increase in air temperature and decrease in precipitation over the last few decades (see Hedding and Greve, 2018; Mélice et al., 2003; Nel et al., 2023; Rouault et al., 2005; Smith, 2002), identifying the drivers behind climate experienced at Marion Island has been shown to be increasingly complex (Toolsee and Lamont, 2022). Similarly, understanding landscape responses, e.g. micro-climate and biotic process, to

regional climatic drivers, in particular the Southern Westerly Winds, are still largely unknown (see Momberg et al., 2021).

2.2. Site selection and sampling

Fieldwork was conducted over the course of three SANAP Marion Island relief expeditions in April/May 2017/18/19 and sampling methods for cosmogenic nuclide exposure dating followed the considerations of Dunai (2010) and others (Ivy-Ochs and Kober, 2008; Masarik and Wieler, 2003). The success of cosmogenic nuclide exposure dating relies heavily on the interpretation of the process-origin of individual samples (Balco, 2011; Dunai, 2010; Hedding et al., 2018). Rudolph et al. (2021a) provides a comprehensive inventory of Marion Island's glacial features and their process-origins, which was used as a foundation for site selection. To supplement existing data (see Rudolph et al., 2020), sites were selected from a range of glacial erosional (e.g. glaciated bedrock) and depositional (e.g. moraine boulders) features, including a dilatation outcrop, distributed across the northern, south-eastern, southern and western sectors of the island (Fig. 1 D). Sample locations were determined with a handheld GPS (Table 1). Approximately 30 x 20 × 2 cm of surface rock was extracted using a battery-operated grinder with diamond-tipped blade, hammer and chisel. Sampling surfaces were no steeper than 20° to avoid, as far as possible, the influence of local shielding, surface erosion (such as pitting) or edge effects. A high-resolution digital surface model (1 × 1 m cell-size; 0.7 m vertical accuracy) was used in ArcGIS to determine site elevation and topographic shielding following the methods of Li (2018) (Table 1). Where applicable, local shielding by, for example, nearby boulders, was also corrected for following the method modified from Balco (2014). Sites and samples were named alphanumerically (see Fig. 1 D and Table 1): the first two letters with reference to the nearest landmark (e.g., Long Ridge = LR); a site number (i.e., 1, 2, 3 etc.) identifying samples with the same (anticipated) exposure age and; a sample duplicate identifier (A, B, C etc.). In practicality, however, topographical differences between sites (e.g., altitude, horizontal distance) can produce large enough error ranges in exposure age determinations to warrant duplicates being re-considered as separate individual sites (e.g. LR3A, LR3B and LR3C, Table 1). A total of thirty-three rock surfaces were sampled at fifteen sites. An average of two samples were collected for each site, but on occasion one or up to three samples were extracted depending on whether surfaces suitable for cosmogenic nuclide sampling could be found (Table 1).

2.3. Site description

Two sites were sampled along Long Ridge, a distinctive wedge-shaped massif on the island's north-east coast that is ~5 km long with cliff faces which are often more than 100 m tall (Figs. 1 and 2). The ridge extends from the Central Highland at 500 m a.s.l. as a tall and narrow feature (Long Ridge South) and gradually lowers and widens towards the coast at 100 m a.s.l. where it becomes more vegetated and covered in platy till material and large boulders (referred to as Long Ridge North) (Fig. 2 A and E). Distinctive moraines are found along either side of the toe end of the ridge, whereas striations and roche moutonnées are found in its higher reaches (Fig. 2 A and B). The ridge is considered as an ice divide separating palaeo-glaciers that had flowed from the interior (Rudolph et al., 2021a). Three boulders were sampled along the inner moraine sequence on the north-western flank of Long Ridge North (LR1A-C) and three striated bedrock surfaces were sampled at Long Ridge South (LR3A-C) (Fig. 2 B and F). The moraines on the steeper south-eastern slope of Long Ridge North were not sampled as post-depositional movement of these boulders is considered very likely.

A further four sites were sampled in the eastern sector. Two depositional sites were sampled at Albatross Lakes (MB1) and Kerguelen Rise (KG1) (Fig. 1). Albatross Lakes is a well-vegetated complex of glacio-genic mounds and ridges, or hummocky terrain, found inland of
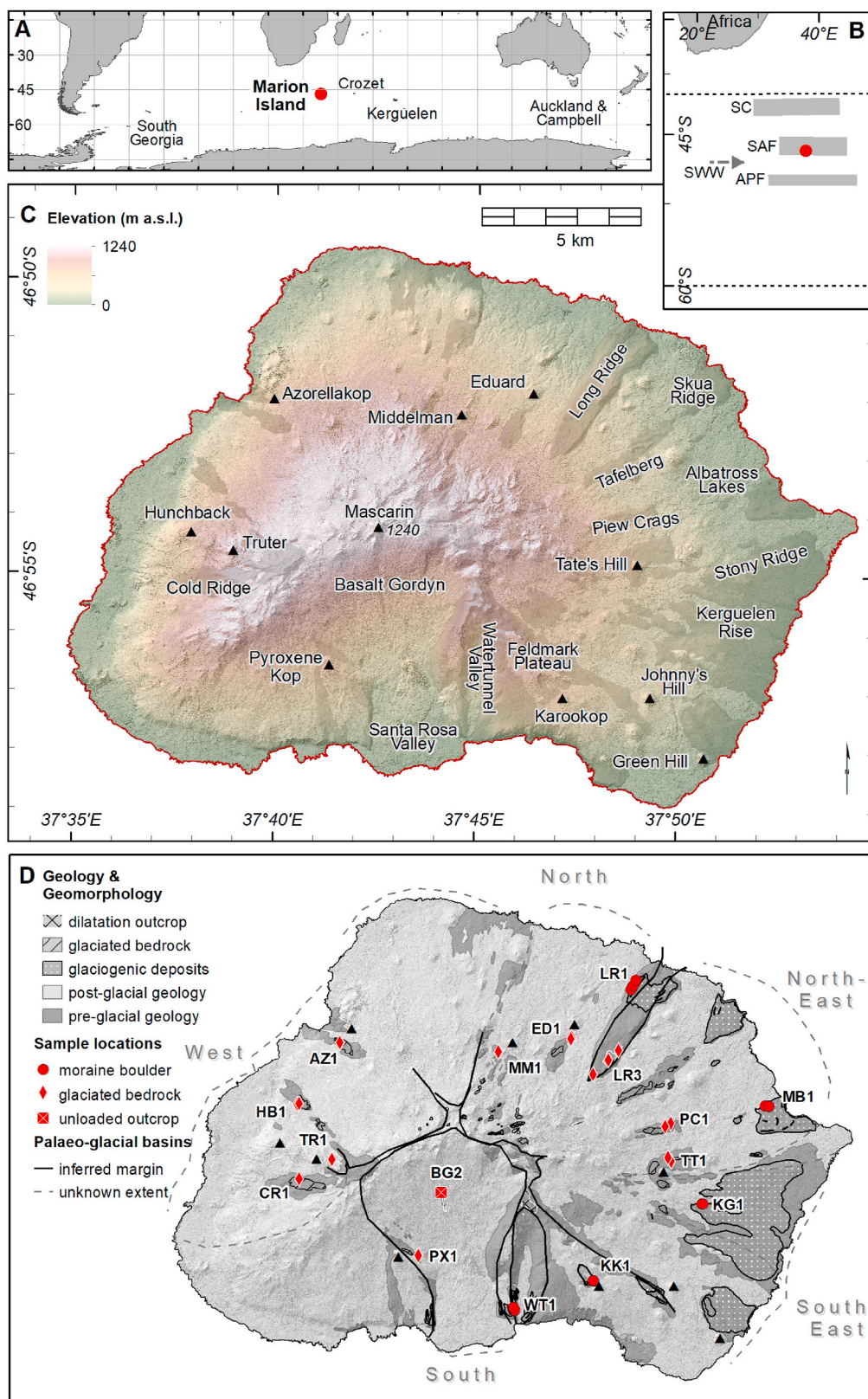
Fig. 1. (A) The greater geographic context of Marion Island. (B) The modern-day latitudinal range of oceanic fronts: Subtropical Convergence (SC); Sub-Antarctic Front (SAF) and Antarctic Polar Front (APF) (Lutjeharms and Ansorge, 2008); and the range extent (black dashed line) and core (grey arrow) of the Southern Hemisphere Westerly Winds (SWW) (Toggweiler and Russell, 2008) in relation to Marion Island. (C) The island topography and a few relevant place names and peaks (▲) (Rudolph et al., 2022b). (D) The distribution of prominent glaciogenic erosional and depositional features found within the island's pre-glacial geological surfaces, adapted from Rudolph et al. (2021a, 2021b) and the location of sample sites and their identifiers (see also Table 1). The island is subdivided into sectors based on an interpretation of palaeo-glacial basins as shown from inferred glacial margins, adapted from Rudolph et al. (2022a).

Table 1

Attribute data and calculated shielding factors (correcting for topographic and local shielding) for the various sample points. Refer to Figs. 1 and 3 and Table 3 for sample locations and exposure age determinations. Sample types include glaciated bedrock surfaces (bedrock), dilatation outcrops (outcrop) and moraine boulders (boulder).

| Sample	Lat. (D.D°)	Long. (D.D°)	Elev. (m)	Bulk dens. (g/cm3)	Thickness (cm)	Shielding Factor	Sample Type
AZ1A	−46.87205	37.66058	369	2.67	1.66	0.9977	bedrock
AZ1B	−46.87195	37.66053	367	2.58	1.55	0.9975	bedrock
BG2B	−46.92111	37.70979	737	1.85	2.4	0.9972	outcrop
BG2C	−46.92113	37.70976	736	2.42	2.38	0.9868	outcrop
CR1A	−46.91701	37.64137	663	2.22	2.7	0.9972	bedrock
ED1A	−46.86970	37.77198	335	2.60	1.35	0.9985	bedrock
ED1C	−46.87008	37.77145	345	2.83	1.76	0.9988	bedrock
HB1A	−46.89235	37.64028	419	2.50	1.21	0.9802	bedrock
HB1B	−46.89227	37.64113	422	2.43	1.23	0.9802	bedrock
KG1B	−46.92405	37.83525	236	2.42	1.3	0.9997	boulder
KG1C	−46.92408	37.83554	234	2.01	1.4	0.9637	boulder
KK1A	−46.94988	37.78341	489	2.61	2	0.9971	boulder
KK1B	−46.94977	37.78325	484	2.60	1.8	0.9974	boulder
LR1A	−46.85360	37.80017	149	2.60	1.2	0.9953	boulder
LR1B	−46.85237	37.80090	127	2.93	1.8	0.9988	boulder
LR1C	−46.85048	37.80222	108	2.27	1.8	0.9970	boulder
LR3A	−46.88176	37.78222	509	2.15	4	0.9872	bedrock
LR3B	−46.87699	37.78967	428	2.33	2.2	0.9992	bedrock
LR3C	−46.87369	37.79448	353	2.60	2	0.9932	bedrock
MB1A	−46.89147	37.86568	42	2.84	0.98	0.9993	boulder
MB1B	−46.89157	37.86523	38	3.00	1.44	0.9762	boulder
MB1C	−46.89162	37.86682	39	3.13	1.33	0.9994	boulder
MM1A	−46.87461	37.73663	567	2.14	1.99	0.9677	bedrock
PC1A	−46.89761	37.81991	314	2.60	1.5	0.9973	bedrock
PC1B	−46.89872	37.81717	338	3.06	1.8	0.9941	bedrock
PX1B	−46.94201	37.69915	399	2.15	1.88	0.9583	bedrock
PX1C	−46.94195	37.69911	400	2.20	1.99	0.9953	bedrock
TR1A	−46.91060	37.65702	841	1.98	2.6	0.9947	bedrock
TR1B	−46.91056	37.65709	838	2.43	2.5	0.9334	bedrock
TT1A	−46.91012	37.82038	337	2.38	1.42	1	bedrock
TT1C	−46.90890	37.81878	341	1.90	1.2	0.9988	bedrock
WT1B	−46.95963	37.74557	118	3.16	1.2	0.9971	boulder
WT1C	−46.95878	37.74506	133	2.60	1.8	0.9978	boulder

Macaroni Bay. It is still uncertain whether or how the ridges could be used to interpret marginal positions of ice extent, but in the least represent areas of ice stand stills (see Rudolph et al., 2022a, 2021a). The only boulders found fit for cosmogenic sampling are located on the northern reaches of the complex - the rest of the material are too weathered. Three boulders were sampled along a crescentic ridge which Rudolph et al. (2021a) previously associated with Hall's (1978) 'moraine sequence 3' (MB1A-C). Farther along the south-east coast, very few boulders within the glaciogenic sediments are suitable for sampling. The material is either very weathered, completely vegetated or has potentially been disturbed by post-depositional slope processes, fluvial processes or scoria eruptions. These conditions are particularly applicable to the deposits of Stony Ridge and Kerguelen Rise that are lower than 200 m a.s.l including the sediments and moraines near the scoria cones of Green Hill and Johnny's Hill (see Fig. 1 C). At higher elevations (above 200 m a.s.l.) boulders on Kerguelen Rise are more intact, embedded, or still perched above the ridge's surface and there is much less vegetation. Two boulders were sampled in the upper reaches of Kerguelen Rise (KG1B & KG1C) (Fig. 1 and Table 1). Another two sites were sampled from erosional features at Piew Crags (PC1) and Tate's Hill (TT1). Piew Crags is a massif of ~1.5 km in length running from west to east, with steep cliffs of >40 m in height. The outcrop is free of vegetation and comprises striae, till and erratic material and joint weathering is also evident. Two surfaces with evidence of abrasion and plucking processes were sampled ~30 m apart from one another (PC1A & PC1B). Similar to Piew Crags, two samples were collected from the striated portions of two adjacent roche moutonnées surrounding Tate's Hill (TT1A & TT1C) (Fig. 1 and Table 1).

Along the south coast, two depositional sites were sampled: a terminal moraine on the Feldmark Plateau near Karookop (KK1A & KK1B) and a lateral moraine in the Watertunnel Valley (WT1) (see Boelhouwers et al., 2008) (Fig. 2 G). The Watertunnel Valley is a small, but well-confined glacial trough with a series of lateral moraines at either side of the valley mouth. A single moraine on the western flank of the valley was sampled (WT1B & C) as the moraines on the eastern side of the valley have been disturbed by post-depositional fluvial processes and were not suitable. Also on the south coast, two sites were sampled in the Santa Rosa Valley basin: two bedrock samples from a roche moutonnée adjacent to Pyroxene Kop (PX1B & C) and two from a dilatation outcrop within the Basalt Gordyn (BG2B & C), the latter of which may or may not be attributed to glacial unloading (Fig. 2 E). On the west and north coast sectors, several glacially-polished outcrops with striations, grooves and a number of roche moutonnées are found above 400 m a.s.l. Some outcrops exhibit plucked faces of >5 m downstream of the abraded surfaces and occasionally erratics of >0.5 m are found. In the west specifically, surfaces often have deeply weathered joints and signs of exfoliation. Two samples were collected from sites with similar appearance near the scoria cones of Eduard (ED1), Truter Peak (TR1), Azorellakop (AZ1) and Hunchback (HB1) while only one sample was collected near Middelman (MM1) and on Cold Ridge (CR1) (Fig. 2 C and D, Table 1).

2.4. Analysis of in situ cosmogenic ^{36}Cl and exposure age determination

Sample preparation and in situ ^{36}Cl analysis were done at the Scottish Universities Environmental Research Centre (SUERC). Bulk rock samples were crushed and sieved to retrieve a 250–710 μm subset. To remove meteoric Cl and contaminants, a ~50 g aliquot of the sample subset was etched overnight in 2 M HNO_3 and 40% HF, losing ~60% of the sample during the process. Afterwards, major element analysis by ICP-OES was done on a ~0.4 g etched split and an additional ~18 g was retrieved for accelerator mass spectrometry target preparation. The
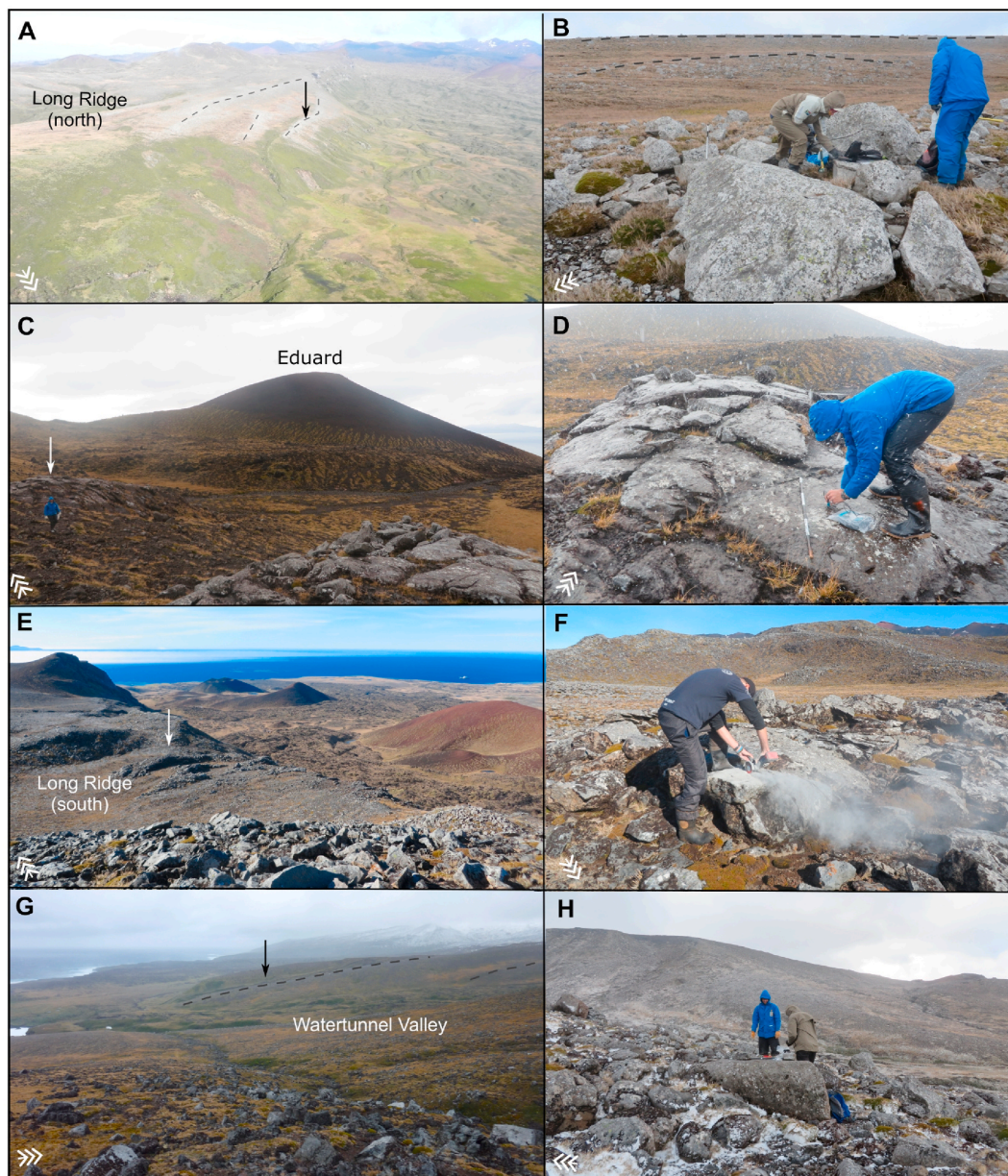
Fig. 2. A few examples of the sites (left) and sampled (right). The single arrow indicates the approximate location of the sampled site (either boulder or bedrock) and the double arrow indicates north. (A & B) Three moraines are found on Long Ridge north (dashed lines), of which three boulders from the inner most moraine was sampled (site LR1). The boulder from LR1C is shown in B. (C & D) Three roche moutonnées were sampled inland from the scoria cone, Eduard (site ED1). The surface of ED1B is shown in D. (E & F) Long Ridge south exhibits several glacially moulded rock surfaces, three surfaces were sampled (LR3), one of which, LR3B, is shown in F. (G & H) Three boulders were sampled form a single moraine it he Watertunnel Valley (WT1), the boulder from WT1C is shown in H. Refer to Fig. 1 for place names and location of sampling points.

samples and two blanks were dissolved in HF with ^{35}Cl enriched spike (~99%) and prepared according to the methods of Marrero (2012). For analysis by AMS, chlorine was extracted and purified to prepare an AgCl target. Targets were pressed into a copper cathode for ^{37}Cl/^{35}Cl and ^{36}Cl/^{35}Cl ratio determination with the 5 MV accelerator mass spectrometer at SUERC. Sample geochemistry and measured ratios are given in Tables 2 and 3. The web-based calculator CRONUScalc v2.1 (Marrero et al., 2016a) was used to calculate exposure ages using the default ^{36}Cl production rates and calibration data, 'SA' scaling (Lifton et al., 2014) and a high-energy neutron attenuation length of 160 g cm^{-2} (Marrero et al., 2016b). The CRONUScalc input files are available online (Rudolph et al., 2023). The effect of snow cover and erosion rates on surface exposure ages at Marion Island are considered negligible (Rudolph et al., 2020).

3. Results

The ^{36}Cl surface exposure age determinations are presented in Table 3 and Fig. 3. In the northern and north-eastern sector, boulder exposure ages from moraine sites at Long Ridge north (LR1, n = 3) and Macaroni Bay (MB1, n = 3) do not produce consistent exposure ages within 1 sigma (1σ) (Table 3). At these sites, we consider the geomorphic context of associated bedrock exposure ages at higher-altitude surfaces to discriminate outliers. The striated surfaces at Eduard (ED1) and Tate's Hill (TT1) are located ~340 m a.s.l. and are associated with the moraines at LR1 and MB1, respectively (Table 3 and Figs. 1 and 2). The exposure ages from ED1 (n = 2) and TT1 (n = 2) are consistent within 1σ and can, therefore, be used to calculate a reliable site exposure age from the arithmetic means of the exposure ages and uncertainties. In both
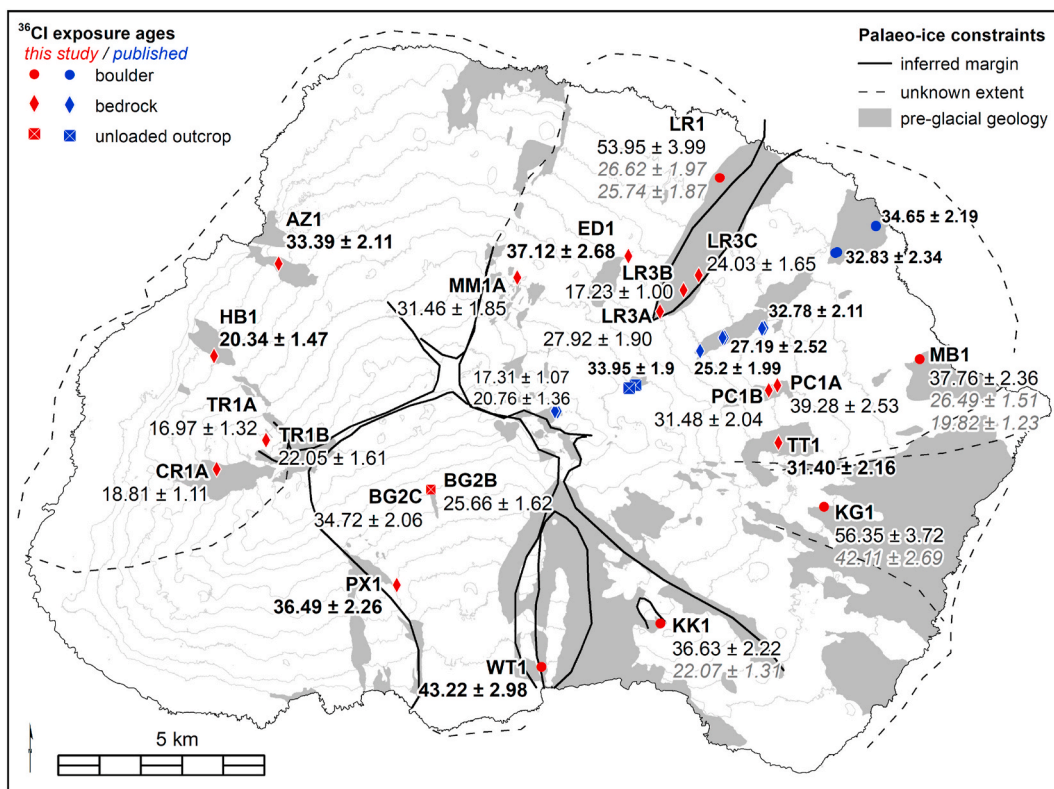
Fig. 3. The ^{36}Cl exposure ages (in ka) of moraine boulders, glaciated bedrock and unloaded (dilatation) outcrops from this study and previously published work (Rudolph et al., 2020). Accepted ages are given in normal font or in bold as the arithmetic mean of two samples, whereas rejected ages are given in grey italics (refer to Table 3). Inferred margins of palaeo-ice extent are shown as adapted from Rudolph et al. (2022a). These spatial and temporal datasets are used to conceptualise an island-scale deglaciation sequence (see Fig. 5).

Table 2
Chemical composition of etched whole rock, including the concentrations of the ^{36}Cl target elements. Chlorine isotopic data are presented in Table 3.

Sample	SiO$_2$ wt (%)	Al$_2$O$_3$ wt (%)	Fe$_2$O$_3$ wt (%)	CaO wt (%)	TiO$_2$ wt (%)	MgO wt (%)	K$_2$O wt (%)	MnO wt (%)	Na$_2$O wt (%)
AZ1A	53.24	16.86	9.92	10.36	4.07	3.38	1.03	0.14	1.00
AZ1B	58.57	13.82	10.02	8.72	3.80	2.96	0.96	0.14	1.01
BG2B	66.60	9.23	9.22	5.15	3.53	2.68	1.35	0.14	2.10
BG2C	68.61	8.48	8.87	4.55	3.66	2.51	1.31	0.14	1.87
CR1A	68.02	7.77	7.19	6.63	2.30	4.99	1.44	0.12	1.54
ED1A	57.16	11.47	11.30	8.43	5.19	4.17	1.14	0.15	1.00
ED1C	56.21	12.07	11.40	8.50	5.23	4.18	1.26	0.16	0.99
HB1A	59.74	5.16	10.04	9.05	2.23	12.04	0.94	0.18	0.61
HB1B	76.59	6.47	6.69	2.98	2.45	1.99	1.26	0.11	1.45
KG1B	56.45	12.37	12.21	7.31	5.88	3.26	1.35	0.17	1.01
KG1C	58.17	11.90	11.78	6.96	5.43	3.21	1.39	0.17	0.99
KK1A	70.76	6.21	7.39	5.75	2.20	5.68	0.91	0.12	0.99
KK1B	66.97	9.21	8.38	5.97	3.56	2.86	1.15	0.14	1.76
LR1A	68.60	7.90	9.06	5.58	3.81	2.75	0.78	0.14	1.38
LR1B	59.20	12.55	10.59	7.15	4.83	3.06	1.45	0.16	1.01
LR1C	55.98	14.23	11.65	7.37	5.13	2.94	1.54	0.17	0.99
LR3A	65.20	11.04	7.07	7.81	2.32	3.97	1.02	0.11	1.47
LR3B	52.16	12.10	13.94	7.00	6.47	3.41	1.92	0.22	2.78
LR3C	56.89	17.17	9.98	6.71	3.82	2.28	2.03	0.13	0.99
MB1A	64.65	15.01	5.23	7.71	2.08	1.94	1.32	0.08	1.99
MB1B	81.69	6.16	4.31	2.36	1.40	1.15	1.23	0.08	1.61
MB1C	63.79	9.11	11.22	4.92	4.02	2.98	1.54	0.19	2.23
MM1A	63.35	9.61	10.60	5.34	4.95	2.62	1.26	0.16	2.11
PC1A	60.40	16.11	6.92	9.27	3.25	2.14	0.81	0.10	1.00
PC1B	57.96	17.32	7.58	9.65	3.25	2.34	0.80	0.11	0.99
PX1B	73.75	7.87	5.51	6.08	1.83	3.06	0.78	0.09	1.02
PX1C	74.65	5.90	6.23	5.24	1.85	4.76	0.46	0.11	0.80
TR1A	63.01	7.59	9.38	7.29	2.83	7.31	1.13	0.16	1.31
TR1B	65.84	8.37	10.68	4.95	4.24	2.93	0.96	0.16	1.87
TT1A	56.49	11.45	13.08	7.13	5.36	3.70	1.62	0.18	0.99
TT1C	58.27	9.82	14.11	6.15	4.78	4.14	1.53	0.19	1.01
WT1B	58.42	4.65	11.77	10.65	3.11	9.59	0.63	0.18	1.00
WT1C	55.24	5.59	8.69	14.70	2.94	11.28	0.40	0.16	1.00

Table 3

Chlorine isotopic data with calculated[36]Cl exposure ages and uncertainties reported at 1σ confidence. Analytical uncertainties (in brackets) include uncertainty in the blank and counting statistics. Systematic uncertainties include uncertainty in the[36]Cl production rate. Surface exposure ages in italics are considered outliers. Site ages in bold are arithmetic means of accepted surface ages and uncertainties. See Figs. 1–3 for place names and sample locations.

Sample[a]	Elev. (m)	Sample Mass (g)	Spike mass (mg)	[37]Cl/[35]Cl[a]	[36]Cl/[35]Cl[b]	Bulk Rock Cl[c] (ppm)	[36]Cl[d] (10^3 atoms/g)	Surface Exposure Age (ka)	Site Age (ka)
Northern Sector									
Long Ridge North – lateral moraine									
LR1C	108	12.093	0.3883	0.0656	4.86E-14 ± 1.63E-15	17.50 ± 2.30	171.30 ± 6.71	*26.62 ± 1.67 (1.04)*	
LR1B	127	12.066	0.3499	0.0525	1.03E-13 ± 4.67E-15	5.19 ± 1.57	313.03 ± 14.99	53.95 ± 3.99 (2.77)	53.95 ± 3.99
LR1A	149	18.1844	0.3716	0.099	5.3866E-14 ± 1.675E-15	33.74 ± 2.02	125.10 ± 4.72	*25.74 ± 1.87 (0.99)*	
Eduard – roche moutonnée									
ED1A	335	12.167	0.3872	0.0921	8.18E-14 ± 2.43E-15	45.75 ± 3.65	328.57 ± 11.82	36.81 ± 2.9 (1.32)	**37.12 ± 2.68**
ED1C	345	12.194	0.3939	0.0753	8.52E-14 ± 2.38E-15	27.31 ± 2.78	319.72 ± 10.54	37.43 ± 2.46 (1.27)	
Middelman - roche moutonnée									
MM1A	567	18.6377	0.3714	0.0651	1.1003E-13 ± 3.14E-15	10.92 ± 0.63	221.24 ± 6.56	31.46 ± 1.85 (0.95)	31.46 ± 1.85
North-Eastern Sector									
Macaroni Bay (Albatross Lakes) – deflation moraine									
MB1B	38	18.382	0.3734	0.0559	5.778E-14 ± 1.785E-15	5.45 ± 0.42	106.38 ± 3.62	37.76 ± 2.36 (1.28)	37.76 ± 2.36
MB1C	39	17.9517	0.3742	0.0558	6.3034E-14 ± 1.905E-15	5.54 ± 0.43	119.77 ± 3.96	*26.49 ± 1.51 (0.87)*	
MB1A	42	14.2039	0.3738	0.0687	4.4234E-14 ± 1.372E-15	16.34 ± 0.93	110.11 ± 3.91	*19.82 ± 1.23 (0.68)*	
Piew Crags – glaciated pavement									
PC1A	314	12.324	0.3802	0.0487	8.55E-14 ± 2.62E-15	2.48 ± 1.52	268.19 ± 9.02	39.28 ± 2.53 (1.32)	39.28 ± 2.53
PC1B	338	12.149	0.3817	0.0477	7.07E-14 ± 2.03E-15	1.73 ± 1.51	223.58 ± 7.16	31.48 ± 2.04 (1.03)	31.48 ± 2.04
Tate's Hill - roche moutonnée									
TT1A	337	12.274	0.386	0.0642	7.70E-14 ± 2.03E-15	15.84 ± 2.19	262.84 ± 8.15	33.01 ± 1.95 (1.03)	**31.40 ± 2.16**
TT1C	341	12.335	0.3854	0.0999	6.44E-14 ± 1.93E-15	54.66 ± 4.05	259.31 ± 9.76	29.78 ± 2.36 (1.14)	
Long Ridge South – glaciated bedrock									
LR3C	353	12.285	0.3916	0.0753	5.83E-14 ± 2.36E-15	26.95 ± 2.74	214.42 ± 9.73	24.03 ± 1.65 (1.1)	24.03 ± 1.65
LR3B	428	18.1641	0.3748	0.0776	7.2878E-14 ± 2.145E-15	18.41 ± 1.01	154.32 ± 5.05	17.23 ± 1 (0.56)	17.23 ± 1
LR3A	509	18.3374	0.3673	0.0943	1.0245E-13 ± 3.115E-15	30.46 ± 1.78	240.79 ± 8.28	27.92 ± 1.9 (0.97)	27.92 ± 1.9
Eastern Sector									
Kerguelen Rise - moraine									
KG1C	234	12.165	0.3916	0.0687	7.75E-14 ± 2.32E-15	20.54 ± 2.45	280.66 ± 9.66	*42.11 ± 2.69 (1.45)*	
KG1B	236	12.081	0.3931	0.0636	1.06E-13 ± 3.49E-15	15.82 ± 2.24	381.77 ± 13.81	56.35 ± 3.72 (2.19)	56.35 ± 3.72
Southern Sector									
Watertunnel Valley – lateral moraine									
WT1B	118	12.049	0.3799	0.0505	8.81E-14 ± 2.04E-15	4.00 ± 1.63	285.05 ± 7.55	46.31 ± 3.12 (1.32)	**43.22 ± 2.98**
WT1C	133	12.094	0.3813	0.0488	9.56E-14 ± 2.75E-15	2.62 ± 1.56	307.84 ± 9.73	40.13 ± 2.83 (1.27)	
Karookop – terminal moraine									
KK1B	484	18.6479	0.3704	0.0562	7.9421E-14 ± 2.193E-15	5.48 ± 0.42	146.06 ± 4.35	*22.07 ± 1.31 (0.66)*	
KK1A	489	17.6656	0.3711	0.0591	1.1019E-13 ± 3.161E-15	7.41 ± 0.50	220.47 ± 6.69	36.63 ± 2.22 (1.12)	36.63 ± 2.22
Pyroxene Kop – glaciated pavement									
PX1B	399	18.5556	0.3705	0.0686	9.5061E-14 ± 2.301E-15	12.99 ± 0.73	194.49 ± 5.00	35.65 ± 2.15 (0.92)	**36.49 ± 2.26**
PX1C	400	18.179	0.3675	0.063	8.3117E-14 ± 2.416E-15	9.86 ± 0.59	167.20 ± 5.06	37.32 ± 2.37 (1.14)	
Basalt Gordyn – dilatation outcrop									
BG2C	736	17.87	0.3817	0.0792	1.2325E-13 ± 3.665E-15	21.00 ± 1.15	285.42 ± 9.06	34.72 ± 2.06 (1.12)	34.72 ± 2.06
BG2B	737	18.096	0.3675	0.0619	1.0883E-13 ± 4.056E-15	8.70 ± 0.54	213.26 ± 8.36	25.66 ± 1.62 (1)	25.66 ± 1.62
Western Sector									
Azorellakop - roche moutonnée									
AZ1B	367	12.265	0.3909	0.0643	7.91E-14 ± 2.39E-15	16.15 ± 2.23	278.15 ± 9.55	35.63 ± 2.23 (1.24)	**33.39 ± 2.11**
AZ1A	369	12.055	0.3733	0.0519	8.08E-14 ± 2.31E-15	5.06 ± 1.65	261.50 ± 8.42	31.14 ± 1.99 (1.02)	
Hunchback - roche moutonnée									
HB1A	419	18.2581	0.3737	0.0717	6.8605E-14 ± 2.062E-15	14.53 ± 0.81	139.29 ± 4.61	17.83 ± 1.13 (0.59)	**20.34 ± 1.47**
HB1B	422	18.6288	0.37	0.0995	5.5147E-14 ± 1.673E-15	33.19 ± 2.00	125.03 ± 4.64	22.84 ± 1.8 (0.97)	
Cold Ridge – glaciated bedrock									

Table 3 (*continued*)

Sample[a]	Elev. (m)	Sample Mass (g)	Spike mass (mg)	$^{37}Cl/^{35}Cl$[a]	$^{36}Cl/^{35}Cl$[b]	Bulk Rock Cl[c] (ppm)	^{36}Cl[d] (10^3 atoms/g)	Surface Exposure Age (ka)	Site Age (ka)
CR1A	663	17.8994	0.3689	0.0712	8.4153E-14 ± 2.464E-15	14.32 ± 0.80	173.40 ± 5.53	18.81 ± 1.11 (0.59)	18.81 ± 1.11
Truter Peak - roche moutonnée									
TR1B	838	18.5893	0.3653	0.1014	7.9625E-14 ± 2.186E-15	35.46 ± 2.19	190.59 ± 6.36	22.05 ± 1.61 (0.76)	22.05 ± 1.61
TR1A	841	17.9073	0.3692	0.1034	7.8815E-14 ± 2.222E-15	38.93 ± 2.44	200.21 ± 6.90	16.97 ± 1.32 (0.58)	16.97 ± 1.32

[a] AMS targets were prepared and measured at SUERC.

[b] Normalised to standard Z93-0005 produced at Prime Lab (Purdue University) with a nominal $^{36}Cl/Cl$ ratio of 1.2E-12.

[c] Stable Cl concentrations were calculated by AMS isotope dilution (Di Nicola et al., 2009). All samples were spiked with non-natural Cl with a $^{35}Cl/^{37}Cl$ ratio of 21.52 ± 0.02 atoms/atom.

[d] Procedural blank $^{36}Cl/Cl = 3.46 ± 0.48$ x10^{-15}. Blank corrections for ^{36}Cl concentrations ranged from between 1.5 and 5%.

cases, the calculated exposure age of the higher-altitude bedrock sites are bracketed by the range of the boulder exposure ages of their associated moraines: ED1 (37.12 ± 2.68 ka) relating to LR1A (25.74 ± 1.87), LR1B (53.95 ± 3.99) and LR1C (26.62 ± 1.67); and TT1 (31.40 ± 2.16) relating to MB1A (19.82 ± 1.23), MB1B (37.67 ± 2.36 ka) and MB1C (26.49 ± 1.51) (see Table 3 and Fig. 3). The older boulder ages (LR1B and MB1B) are thus accepted in both cases as more appropriate in the context of their geomorphic association. In addition, we also consider that it is more likely for exposure ages to be under-estimated due to erosion that is (potentially) unaccounted for, rather than over-estimated due to, for example, unaccounted inheritance. We apply the former approach consistently to other moraine sites, specifically for where individual boulder ages do not overlap within 1σ and there are no other geomorphic reasons to discriminate between outliers, by accepting the older exposure ages and rejecting the younger. Examples of these are Kerguelen Rise (KG1B, 56.35 ± 3.72 ka) from the eastern sector and Karoo Kop (KK1A, 36.63 ± 2.22 ka) in the south (Table 3). The exposure age of the roche moutonnée at Middelman (MM1, 37.67 ± 2.36 ka) can broadly be contextualised with its lower lying counterpart, ED1, and is therefore accepted despite having only one age determination (Fig. 3). Other high-lying bedrock sites in the north-eastern sector where individual sample ages do not overlap within 1σ (i.e., at Piew Crags (PC1) and Long Ridge South (LR3)) can be explained by the elevational (topographical) differences between the sample duplicates. This may account for significant differences in the timing of exposure for these sites. For instance, a difference of ~20 m elevation between PC1A and PC1B on Piew Crags and a range of ~150 m between LR3C (lowest) and LR3A (highest) could account for between 3 and 10 ka exposure age difference as these sites lie on an ice-divide (Table 3 and Fig. 3). At these locations we accept all the exposure ages for our reconstruction.

In the southern sector, mean site ages are calculated for the moraine in the Watertunnel Valley (WT1, 43.22 ± 2.98 ka) and the glaciated bedrock near Pyroxene Kop (PX1, 36.49 ± 2.26) where the sample exposure ages all fall within 1σ (Table 3). The dilatation outcrop at 737 m a.s.l. in the Basalt Gordyn (BG2) produced exposure ages of 25.66 ± 1.62 ka (BG2B) and 34.72 ± 2.06 ka (BG2C) which are younger than the lower-lying striated roche moutonnée associated with this glacial basin (PX1B ~36 ka at 400 m a.s.l.). Despite the ~10 ka range of exposure ages, the individual sample ages are both accepted for the purpose of the island-scale reconstruction as they provide a useful minimum age of exposure for the Santa Rosa Valley which has limited alternative temporal constraints (Table 3 and Fig. 3). In the western sector moraine boulders are absent and the samples only include roche moutonnées and glaciated pavements. The samples at Azorellakop (AZ1) and Hunchback (HB1) do not produce consistent exposure ages at 1σ, but individual samples are still within a 2σ range of each other and translate to a mere ~5 ka difference. In the absence of alternative exposure ages at these sites, the calcualted age range is accepted for the current reconstruction and provide an average site age for AZ1 (33.39 ± 2.11 ka) and HB1 (20.34 ± 1.47). The samples from Cold Ridge (CR1, n = 1) and Truter

Peak (TR1, n = 2) do not produce site-specific statistically significant exposure ages. Still, the exposure ages can loosely be contextualised with surrounding site ages (see Fig. 3) and are, thus, all accepted (Table 3).

4. Discussion

4.1. Marion Island's glacial chronology and a-synchronous deglaciation

We present a total of 27 new cosmogenic ^{36}Cl exposure ages combined with those already published for Marion Island (see Rudolph et al., 2020); the probability density functions of which are shown in Fig. 4. Assessing the exposure ages of moraine boulders and bedrock sites separately, can assist in identifying significant peaks in Marion Island's deglaciation chronology. The moraine boulder exposure ages range between ~36 and ~56 ka and are useful to interpret periods of ice advances or stand still events (Fig. 4 B). The bedrock exposure ages range between ~16 and ~39 ka and can signify periods of island-wide retreat (Fig. 4 C). From these, two stand still events are recognised at ~55 ka and ~35 ka ago (Fig. 4 B) and three periods of significant retreat can be seen at ~33 ka, ~25 ka and ~17 ka (Fig. 4 C). The exposure age chronology further suggests that island-scale deglaciation was a-synchronous, more specifically, that the northern, eastern and southern sectors deglaciated much earlier than the north-eastern and western sectors (Fig. 4 D). The lateral moraines in the northern (LR1B, ~54 ka), south-eastern (KG1B, ~56 ka) and southern (WT1, ~43 ka) sectors are significantly older than the coastal deposits in the north-eastern sector of the island at Albatross Lakes (MB1, ~38 ka) (see Figs. 3 and 4 D). The Karookop site (KK1, ~37 ka) in the south is an exception to this trend, as it is similar in age to Albatross Lakes but >440 m higher in altitude. Exposure ages of bedrock surfaces confirm a similar trend of a-synchronicity: northern (ED1, ~37 and MM1, ~31 ka), south-eastern (TT1, ~31 ka) and southern (PX1B, ~36 ka) surfaces were exposed slightly earlier than surfaces at similar altitudes in the north-eastern sector (LR3, ~17–27 ka ago) (Table 3). In addition, the exposure ages of the bedrock in the western sector range between ~16 and 22 ka (HB1, CR1, TR1) suggesting that the western region of the island deglaciated synchronously to the north-eastern sector (Table 3).

4.2. A spatio-temporal reconstruction of Marion Island's deglaciation

Here we present a conceptual model of island-scale deglaciation incorporating the presented findings and previous reconstructions of the temporal and spatial character of Marion Island's palaeo-ice extent (Fig. 5). The extent of palaeo-ice proposed in the model is constrained by a reconstruction of palaeo-ice margins (Rudolph et al., 2022a) which incorporates comprehensive glacial geomorphological mapping (Rudolph et al., 2021a) (see Fig. 1). The chronology combines the deglaciation timeline for the north-eastern sector of the island (Rudolph et al., 2020) with the new chronology presented here (Fig. 3). Site
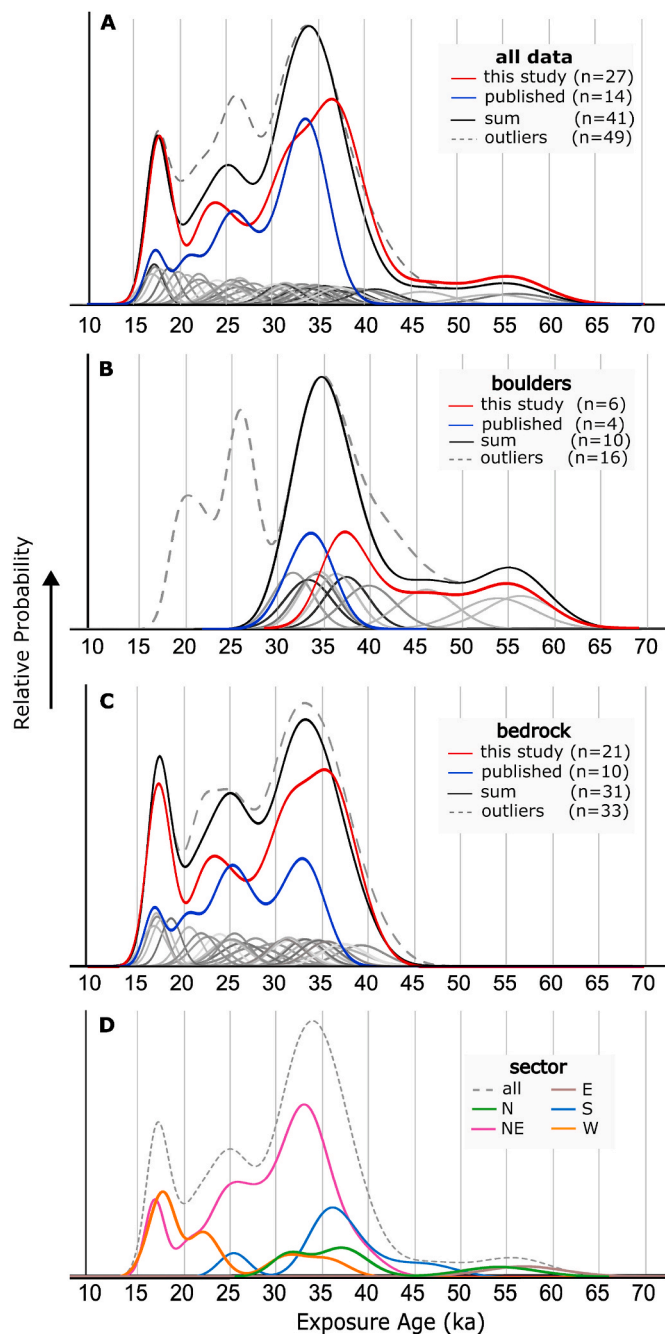
Fig. 4. Probability plots of ^{36}Cl exposure ages for (A) all the sample sites, (B) the moraine boulders and (C) the bedrock sites from this study (red curves) and a previously published data set (blue curves; Rudolph et al., 2020). The plots show the individual exposure ages (grey), the summed probability of individual ages with outliers included (grey dashed curves) and the represent the summed probability of the datasets combined, outliers excluded (black curves). (D) The summed probability of all the accepted exposure ages for the entire island (grey dashed curve) and for different sectors (refer to Fig. 1 for a demarcation of island sectors).

exposure ages (as in Table 3 and Fig. 3) are rounded-off to simplify the final reconstruction (Fig. 5).

We provide the oldest moraine sequences yet dated for the sub-Antarctic islands, at 53.95 ± 3.99 ka and 56.35 ± 3.72 ka, which extends Marion Island's glacial chronology into early MIS 3. This suggests that the last maximum ice extent was reached prior to ~56 ka ago and it is noteworthy to mention that stratigraphically older features have not yet been dated. Consequently, our conceptual reconstruction starts from

the local LGM at ~56 ka ago (Fig. 5 A). Island-scale retreat continued until ~33 ka ago, likely interrupted by localised advances at ~43 ka (Watertunnel Valley moraine) and ice stand stills at ~38 ka (deflation moraine at Macaroni Bay), ~37 ka (terminal moraine at Karookop), ~35 and ~33 ka ago (deflation moraine of Skua Ridge) (Fig. 5 B - C). By ~34 ka ago, bedrock above 900 m a.s.l. was already exposed (Fig. 5 C) and by ~31 ka, the majority of mid-altitude (300–400 m a.s.l.) bedrock surfaces in the north, east and southern sectors became exposed (Fig. 5 D). On the leeward north-east coast, the rate of retreat was slow (~9 km in 17 ka; Rudolph et al., 2020) where bedrock surfaces, at similar altitudes (>300 m a. sl.), were exposed only after 30 ka (Fig. 5 D). On the windward west coast of Marion Island, ice-masses were maintained at elevations above ~400 m a.s.l. until ~20 ka ago after which retreat ensued rapidly (Fig. 5 C and D). This assessment excludes the bedrock near Azorellakop (AZ1), which was exposed earlier (~33 ka, at 369 m a.s.l.) and may be attributed to marginal shrinkage of the ice-mass in this region (as opposed to altitudinal retreat) along the west coast. Island-wide deglaciation continued until ~17 ka, with no evidence of subsequent ice stand stills or re-advances (Fig. 5 D). The pattern of a-synchronous deglaciation is most likely the result of orographic and physiographic effects on precipitation. The relation between the island's distinct physiography (altitude, subaerial extent, surface profile) and geographic location in relation to the Westerly Wind belt of the Southern Hemisphere, ocean fronts and cyclonic systems, has already been identified by previous works (Lamont and Toolsee, 2022; Le Roux, 2008; Schulze, 1971; Smith and Steenkamp, 1990). Still, the interplay of these factors throughout the Quaternary and the effect it has on local equilibrium line altitudes and accumulation area ratios remains to be explored.

It is prudent to note some uncertaintites inherent to this conceptual model: extensive post-glacial vlocanism obscures much of the palaeo-glacial landscape (Rudolph et al., 2021b) leaving large parts of the island open to interpretation, e.g. the west coast (see Fig. 3). Also, the time-slices suggested in Fig. 5 should be viewed in lieu of uncertaintites associated with exposure ages and, in principle, cosmogenic nuclide dating. The reliability of the model can be improved in the future through, for example, multi-proxy approaches, applying different ^{36}Cl production rates or estimating the potential effect of erosion.

4.3. Implications for Marion Island's landscape evolution

Existing interpretations of landscape evolution and ecological succession on Marion Island can be reviewed from site-specific deglaciation patterns. First, it has been proposed that the Watertunnel Valley and a cirque basin near Karookop (or Snok) may have been associated with either the global Last Glacial Maximum (~20 ka ago) or with early Holocene glaciation, while island-wide ice retreat was prevalent (Boelhouwers et al., 2008; Hall et al., 2011). Our results show that the small lateral moraine in the Watertunnel Valley (~43 ka at 120 m a.s.l) and the terminal moraine near Karookop (~37 ka at 470 m a.s.l) pre-dates the global last glacial maxima. In addition, the exposure (formation) ages of the moraines at Karookop and Watertunnel significantly pre-dates the island's youngest constrained retreat sequence (i.e. the Skua Ridge-Tafelberg sequence, 25–35 ka; Rudolph et al., 2020), meaning the cirque at Karookop and the Watertunnel Valley were likely unable to sustain ice throughout island-scale deglaciation. The hypotheses of high-lying outcrops acting as biological refugia during periods of maximum ice extent needs to be revisited. None of the ^{36}Cl exposure ages of bedrock surfaces (including glaciated and non-glaciated) indicate that these features were ice-free nunataks during the local Last Glacial Maximum at ≥56 ka ago, nor soon after. These surfaces, which range between ~300 and 900 m a.s.l., became exposed at the earliest ~39 ka ago when much of the coastal regions were already ice-free (Fig. 5 C). However, geomorphological evidence suggests that the Feldmark Plateau and the mid-section of Long Ridge were ice-free areas (Boelhouwers et al., 2008; Rudolph et al., 2022a; Sumner and Meiklejohn, 2004) (Fig. 4 A). As such, we propose that the massifs of
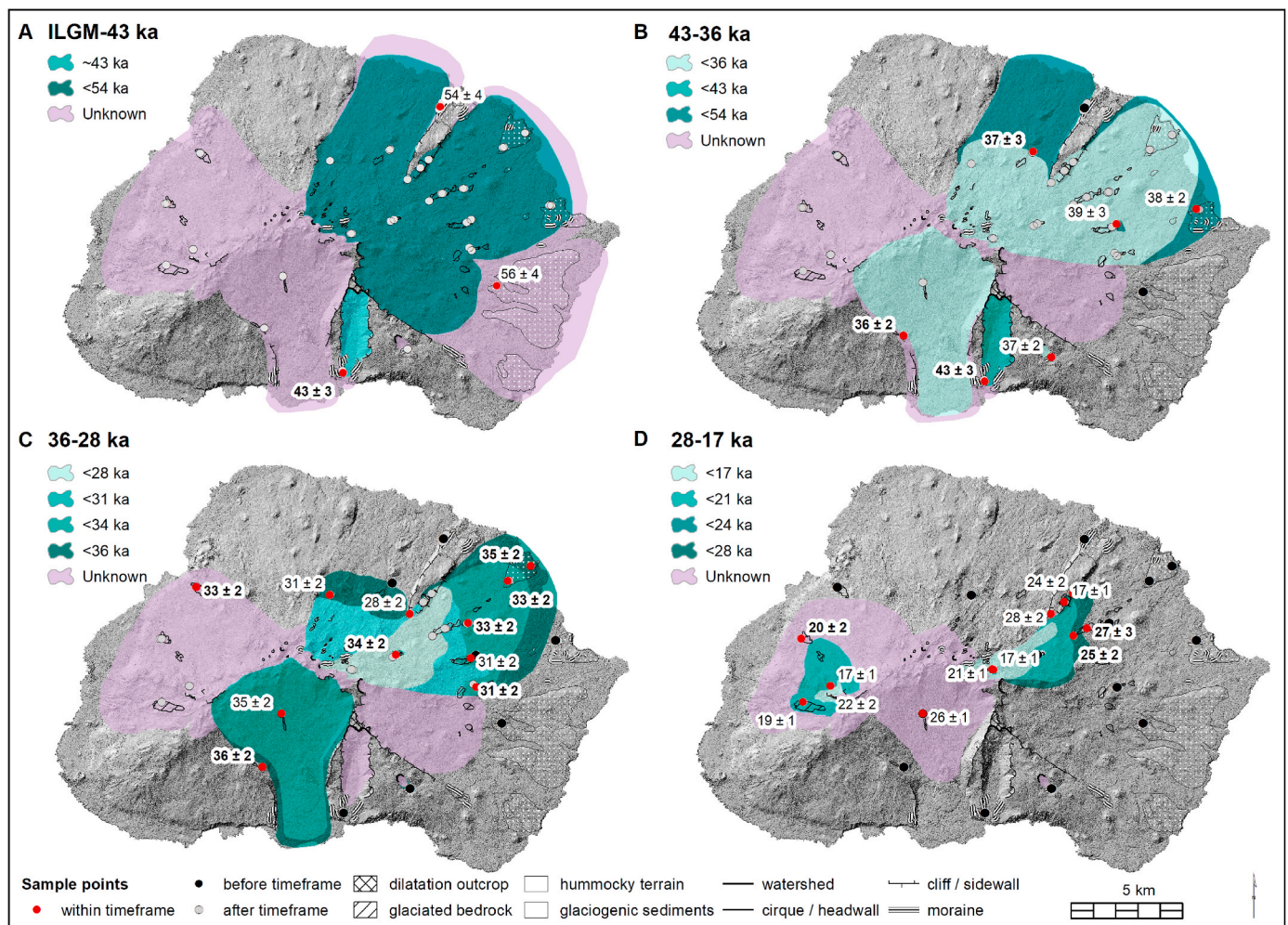
Fig. 5. A conceptual model of island-scale deglaciation across time scales (A) from the interpreted local LGM up to ~43 ka, (B) 43-36 ka ago, (C) 36-28 ka and (D) 28-17 ka ago. The temporal sequence is based on the ^{36}Cl exposure ages from this and prior studies (Rudolph et al., 2020). Exposure ages and uncertainties are rounded-off and given in ka. The spatial interpretation of palaeo-ice extent is based on geomorphological constraints (Rudolph et al., 2021a) and an interpretation of palaeo-glacial basins (Rudolph et al., 2022a). See Fig. 3 for the delineation of inferred and unknown margins and the full suite of exposure ages and uncertainties. Place names are shown in Fig. 1.

Feldmark Plateau and (mid-) Long Ridge are potentially the oldest exposed surfaces on the Island and the most likely candidates for biological refugia along with coastal areas now inundated by post glacial sea level rise. But low-lying ice-free areas would also (or equally) have attributed to the survival of endemic species during maximum glaciation (Rudolph et al., 2020). Lastly, the origin of the Santa Rosa Valley has been debated (see Chevallier, 1986; Hall et al., 2011), but we now provide evidence to support the hypothesis that the expanse of the valley and the dilatation outcrop in the centre of the Basalt Gordyn was glaciated. The exposure age of the striated pavement near Pyroxene Kop (PX1, ~36 ± 2 ka) slightly pre-dates the exposure age of the unloaded outcrop (BG2C, ~34 ± 2 ka) (Fig. 2 E). Either this outcrop has been glaciated or the erosion of the unloading process has removed enough rock material to keep the exposure age at ~36 ka, but not enough to completely reset the age.

4.4. Comparison with other Southern Hemisphere glacial chronologies

A comparison of Marion Island's glacial chronology to those documented elsewhere in the Southern Hemisphere can be seen in Fig. 6. The new ^{36}Cl exposure ages presented here adds to a growing body of evidence showing that sub-Antarctic islands experienced more extensive glacial maxima's during their MIS 3/4 advances than during MIS 2

(global Last Glacial Maximum) or subsequent glaciations (e.g., Antarctic Cold Reversal) (e.g. Darvill et al., 2016; Schaefer et al., 2015; Shulmeister et al., 2019). On the Kerguelen Archipelago, the last maximum ice extent was reached within MIS 3 at ~41 ka ago (Jomelli et al., 2018). This is also the only other sub-Antarctic island to have direct age constraints on its last maximum palaeo-ice extent (Petherick et al., 2022). On South Georgia (Bentley et al., 2007; Hodgson et al., 2014a; Lešić et al., 2022; White et al., 2018) and Auckland and Campbell Islands (Rainsley et al., 2019), a variety of proxy evidence and modelling approaches also indicate that a more extensive glaciation was reached during MIS 3 and less extensive advances during MIS 2. The pattern from regional summaries of Patagonia and New Zealand is also broadly comparable to that of the sub-Antarctic islands (Fig. 6). In the Southern Hemisphere, palaeo-ice extent during MIS 3 or MIS 4 glaciations were generally more extensive or equal to that of MIS 2 (Darvill et al., 2016), with the exception of New Zealand's central South Island (Shulmeister et al., 2019). Noteworthy differences between the chronologies of these locations are apparent in the local significance of the MIS 2 advances. On South Georgia and the Kerguelen Archipelago, where ice caps persist today, and on the larger continental ice field of Patagonia and New Zealand, evidence of the MIS 2 advances are abundant. Conversely, on the currently ice-free islands of Marion, Auckland and Campbell, evidence for the MIS 2 advances is limited. There is thus clearly local (likely
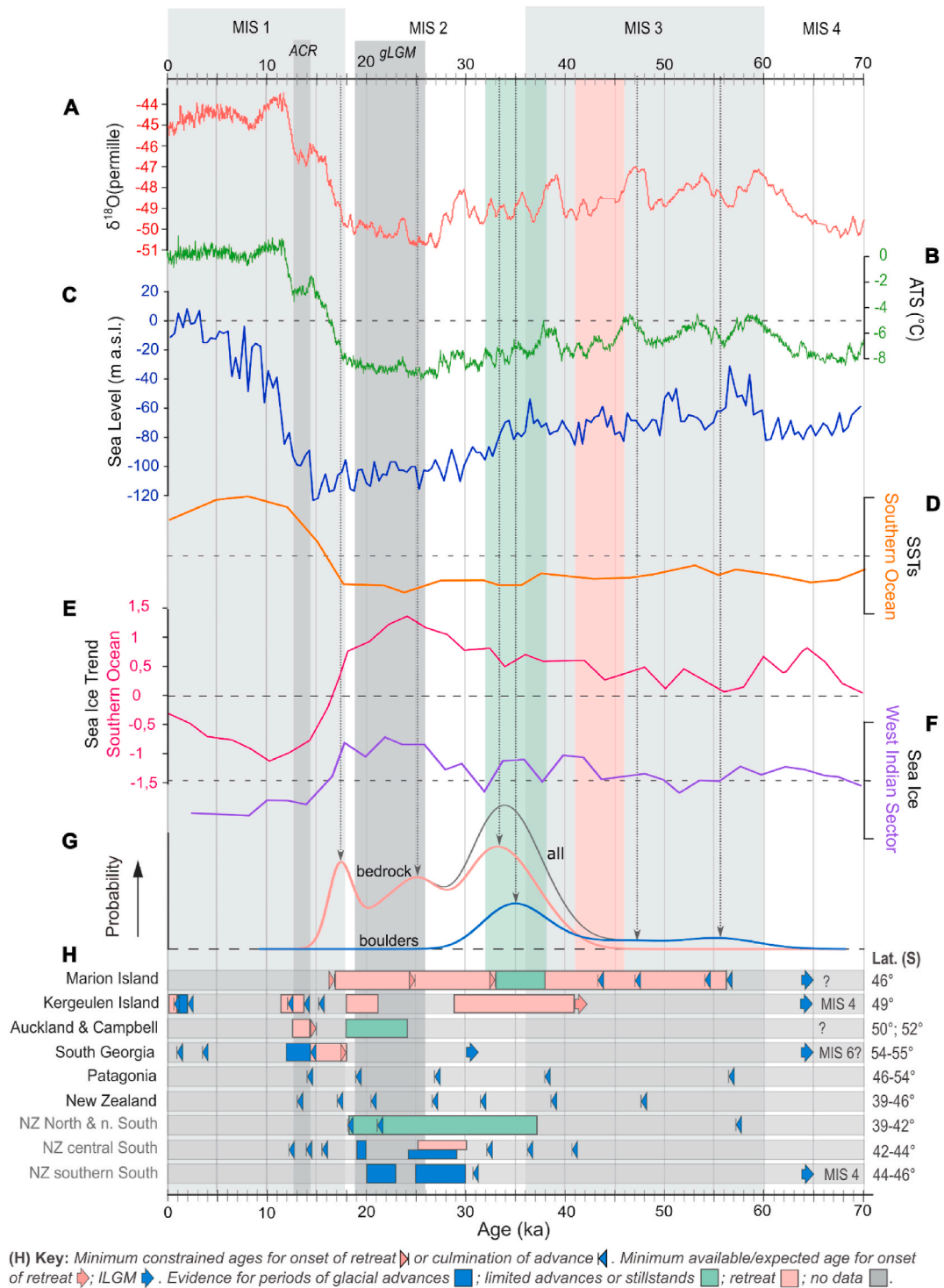
Fig. 6. Southern Hemisphere glacial chronology juxta-posed next to several climatic proxies, adapted form the original works as indicated: (**A**) δ^{18}O record from Dronning Maud Land, Antarctic (EPICA, 2006); (**B**) Antarctic Temperature Stack (ATS) in change relative to present day temperatures (Parrenin et al., 2013); (**C**) Global Mean Sea Level relative to present day sea level (Miller et al., 2020); Adapted from Chadwick et al. (2022) are (**D**) the Southern Ocean Sea Surface Temperatures (SSTs); (**E**) the dominant trend in Southern Ocean sea ice extent and (**F**) sea ice extent for the Western Indian Ocean sector. (**G**) Probability plots of [36]Cl exposure ages from this study and Rudolph et al. (2020) for moraine and glaciated bedrock sites. (**H**) A comparison of glacial chronologies from other Southern Hemisphere regions with their latitudinal ranges: Kerguelen Archipelago, main island (Charton et al., 2021, 2022; Jomelli et al., 2017, 2018); Auckland and Campbell Island (Rainsley et al., 2019), South Georgia (Bentley et al., 2007; Graham et al., 2017; Hodgson et al., 2014a; Lešić et al., 2022; White et al., 2018) and regional reviews of Patagonia (Darvill et al., 2016) and New Zealand (Shulmeister et al., 2019). The chronostratigraphic units are from Railsback et al. (2015) (MIS), Clark et al. (2009) (gLGM) and Putnam et al. (2010) (ACR), adapted form Rudolph et al. (2020). (Refer to Web version of this article for colour interpretation).

a combination of latitudinal position, sub-aerial extent and maximum elevation) as well as regional controls on the glaciations of sub-Antarctic islands.

4.5. The role of regional climate

Overall, the glacial chronologies reconstructed for the sub-Antarctic islands and the regional reviews are broadly consistent with the Antarctic temperature record from Dronning Maud Land (EPICA, 2006) (Fig. 6 A and H). For regions where glacial maxima or advances are documented within MIS 4 (Darvill et al., 2016; De Deckker et al., 2019; Schaefer et al., 2015) the timing thereof (~65 ka) correlates to a period when Antarctic temperatures reached a minimum anomaly of −8 °C – following long-term cooling of the Southern Hemisphere from MIS 5.1/5a (Jouzel et al., 2007; Railsback et al., 2015) (Fig. 6). Such advances are so far only documented in continental mountain regions of the Southern Hemisphere (Darvill et al., 2016; Schaefer et al., 2015; Shulmeister et al., 2019), and are anticipated for several sub-Antarctic islands through proxies or where glaciers were most likely marine terminating e. g South Georgia (Hodgson et al., 2014a; Lešić et al., 2022), Marion Island (Hodgson et al., 2014b; Rudolph et al., 2020), Auckland and Campbell Islands (Rainsley et al., 2019) and potentially Kerguelen (Jomelli et al., 2018). By MIS 3, temperatures were warmer and very variable resulting in retreat from glacial maxima (~46-41 ka) and frequent, but localised, oscillations in glacier ice extent (~38-32 ka). This likely reflects an increasing influence of local factors such as the position of the Southern Westerly Winds, sea ice extent and sea levels as well as local orography and physiography on moisture delivery and glacial mass balance (e.g. Chadwick et al., 2022; Lenaerts et al., 2014; Miller et al., 2020; Sime et al., 2013) (Fig. 6). These signatures are especially clear when assessing the response of individual glacier outlets or isolated mountain valleys across the Southern Hemisphere (Eaves et al., 2016, 2019; García et al., 2018; Mackintosh et al., 2006). Higher altitude or colder mountain regions seem to have maintained their glaciers throughout this period (due to a favourable altitude-precipitation relationship and its impact on equilibrium line altitudes) with advances (possibly) corresponding to MIS 3 temperature and summer insolation minima's (~41 and ~32 ka) (Jouzel et al., 2007; Petherick et al., 2022). During MIS 2 with temperatures still decreasing between 30 and 28 ka, extensive sea ice (Chadwick et al., 2022; Sime et al., 2016) potentially starved some of the lower lying valleys and mid-latitude sub-Antarctic islands of moisture. This resulted in limited ice advances or complete still stands on, for example, Marion Island, Auckland and Campbell and Kerguelen etc. whereas at the higher latitudes and altitudes of South Georgia, Patagonia and New Zealand, favourable conditions allowed for extensive glacial advances.

The reasons for differences in ice extent of regional glaciations during MIS 4 and MIS 2 is most likely due to the characteristics of the Southern Ocean and the position of the Southern Westerly Wind belt and their potential to provide sufficient moisture during these two periods (Chadwick et al., 2022; De Deckker et al., 2019; Schaefer et al., 2015). For instance, during MIS 4, sea ice was less extensive than in MIS 2 (Chadwick et al., 2022). With more open ocean available in MIS 4, moisture delivery would have been enhanced; especially to the sub-Antarctic islands with hyper-maritime climates. At continental landmasses that are less dependent on sea surface characteristics, extensive sea ice in MIS 2 would not have had as significant an effect on inhibiting moisture delivery as at the sub-Antarctic islands. Furthermore, global eustatic sea level was higher in MIS 4 (only −70 m) as compared to MIS 2 (−140 m) (Miller et al., 2020) which affected precipitation delivery as well as equilibrium line altitudes (ELAs). This effect would have been more pronounced at relatively lower altitude sub-Antarctic islands as compared to continental land masses (e.g. Patagonia and New Zealand) where isostatic compression would reduce the range of ELAs between MIS 4 and 2. A lowering of ELA can have a positive or negative feedback effect on glacial mass balance, depending

on the local physiography (aspect or relief) (Benn and Evans, 2014). The track of the Southern Westerly Wind belt also affects the amount and type of moisture delivery to landmasses across the Southern Ocean. Typically, under colder conditions with a northward shift of the wind belt, cold Antarctic air brings snow to high mountainous regions. During warmer interglacial periods, a southward shift of the winds pulls sub-tropical air mases south, bringing rain (Crosta et al., 2004; Gersonde et al., 2005). During MIS 4, the northward shift of the westerlies, coupled with open ocean would have provided sufficient snowfall to (continental) landmasses to advance glacial ice. During MIS 2, while air temperatures would have been cooler and the Southern Westerly Wind belt extended northwards, extensive sea ice would not have necessarily inhibited moisture delivery to large continental ice sheets which cover a broader latitudinal range (e.g. Bendle, 2021; De Deckker et al., 2019; Shulmeister et al., 2019), but would effectively have starved the sub-Antarctic islands of their atmospheric moisture resulting in minor ice advances or still stands.

4.6. Future directions

There are still several challenges that limit a holistic spatial and temporal interpretation of island-scale deglaciation for Marion Island. The current dataset does not allow for interpretations on periods earlier than 56 ka or between 54 and 43 ka, and 43 - 39 ka and younger than 17 ka. Geomorphological evidence in the form of marginal moraines do exist that may be attributed to these periods, but most are unsuitable for current cosmogenic nuclide exposure dating capabilities. Examples of these are the moraine sequences on the southern flank of Long Ridge North and the outer moraines on the northern flank of Long Ridge North, deposits near Johnny's Hill and marginal moraines on either side of the valleys of Santa Rosa and Watertunnel. Other glacial termini will most likely be found submerged offshore on the east coast (Hodgson et al., 2014b) but the character and form of such offshore termini still remain to be investigated and mapped. Future terrestrial campaigns might focus on features found in the Central Highland of the island which will aid in reconstructing the Holocene glacial chronology, whereas the age and development of periglacial features might assist in answering altitudinal temperature trends and reconstructing equilibrium line altitudes. For regional reconstructions, evidence for a ~32 ka or ~21 ka cold period (see Petherick et al., 2022) is absent at Marion Island and they are not particularly apparent in other mid-latitude sub-Antarctic islands. It is, therefore, prudent to consider the effects of variability in glacial chronologies at a smaller scale when untangling Hemispheric climatic drivers from reconstructed regional chronologies.

5. Conclusion

Cosmogenic ³⁶Cl-exposure ages of glacial features on Marion Island provides the oldest dated terrestrial moraine sequences for the sub-Antarctic islands with the culmination of ice advances at ~56 ± 4 ka and a localised re-advance at ~43 ± 3 ka ago. From our dataset, localised stand stills are interpreted for between ~38 ± 2 and ~33 ± 2 ka, with a general trend of retreat throughout the global LGM until ~17 ka ago. Any ice re-advances during the Antarctic Cold Reversal (15-13 ka) or Holocene cold periods, would have been limited to the Central Highland above 900 m. a.sl. Sites previously associated with Holocene advances, e.g. the terminal moraine at Snok, are shown to be the product of earlier (>MIS 3) advances. Our spatio-temporal reconstruction suggests that the oldest exposed surfaces on the island, and likely candidates for biological refugia, are coastal moraines. High-lying regions such as the Feldmark Plateau and the mid-sections of Long Ridge still require temporal constraints of their exposure. Island deglaciation was asynchronous – attributed to local island physiography and regional climatic variations. The presented ³⁶Cl exposure ages add to a growing body of evidence showing that sub-Antarctic islands experienced more extensive glacial maxima's during their MIS 3/4 advances than during MIS 2

(gLGM) or subsequent glaciations (e.g., ACR) (e.g. Darvill et al., 2016; Schaefer et al., 2015; Shulmeister et al., 2019). Since these finding is most likely due to the characteristics of the Southern Ocean and the position of the Southern Westerly Wind belt and their potential to provide sufficient moisture during these periods, more research is needed to determine of the latitudinal position of the Southern Westerly Wind belt since MIS4. We suggest that variability in deglaciation chronologies at smaller scales, particularly at sub-Antarctic islands, are important to consider when untangling climatic drivers across the Southern Ocean.

Author contributions

All of the authors have made a substantial contribution to this paper and approved the final version of the manuscript. The authors' contributions appear below as per CRediT guidelines: Elizabeth M. Rudolph – Conceptualization; Methodology; Formal analysis; Investigation; Data curation; Writing (original draft); Visualization: David W. Hedding – Methodology; Investigation; Resources; Writing (review & editing); Visualization; Funding Acquisition: Dominic A. Hodgson - Validation; Writing (review & editing); Derek Fabel – Methodology; Resources: Delia M. Gheorghiu – Methodology; Formal analysis; Data curation; Writing (review & editing): Richard Shanks – Formal analysis: Werner Nel – Investigation; Resources; Validation; Writing (review & editing); Funding Acquisition.

Declaration of competing interest

The authors declare that they have no known competing financial interests or personal relationships that could have appeared to influence the work reported in this paper.

Data availability

Data have been uploaded to Mendeley data and a link is provided in the manuscript

Acknowledgements

References

Balco, G., 2011. Contributions and unrealized potential contributions of cosmogenic-nuclide exposure dating to glacier chronology, 1990-2010. Quat. Sci. Rev. 30, 3–27. https://doi.org/10.1016/j.quascirev.2010.11.003.

Balco, G., 2014. Simple computer code for estimating cosmic-ray shielding by oddly shaped objects. Quat. Geochronol. 22, 175–182.

Bendle, J., 2021. The Westerly Winds and the Patagonian Ice Sheet. Roy. Hollow. Univ. London (webpage) URL. https://www.antarcticglaciers.org/glacial-geology/patagonian-ice-sheet/westerly-winds-patagonian-ice-sheet/.

Benn, D., Evans, D.J.A., 2010. Glaciers and Glaciation, second ed. Routledge. https://doi.org/10.4324/9780203785010.

Bentley, M.J., Evans, D.J.A., Fogwill, C.J., Hansom, J.D., Sugden, D.E., Kubik, P.W., 2007. Glacial geomorphology and chronology of deglaciation, South Georgia, sub-Antarctic. Quat. Sci. Rev. 26, 644–677. https://doi.org/10.1016/j.quascirev.2006.11.019.

Boelhouwers, J., Holness, S., Sumner, P., 2003. The maritime Subantarctic: a distinct periglacial environment. Geomorphology 52, 39–55. https://doi.org/10.1016/s0169-555x(02)00247-7.

Boelhouwers, J., Meiklejohn, I., Holness, S., Hedding, D.W., 2008. Geology, geomorphology and climate change. In: Chown, S.L., Froneman, P.W. (Eds.), The Prince Edward Islands: Land-Sea Interactions in a Changing Ecosystem. SUN PRESS, Stellenbosch, pp. 65–96. https://doi.org/10.18820/9781928357063/04.

Chadwick, M., Crosta, X., Esper, O., Thöle, L., Kohfeld, K.E., 2022. Compilation of Southern Ocean sea-ice records covering the last glacial-interglacial cycle (12–130 ka). Clim. Past 18, 1815–1829. https://doi.org/10.5194/cp-18-1815-2022.

Charton, J., Jomelli, V., Schimmelpfennig, I., Verfaillie, D., Favier, V., Mokadem, F., Gilbert, A., Brun, F., Aumaître, G., Bourlès, D.L., Keddadouche, K., 2021. A debris-covered glacier at Kerguelen (49°S, 69°E) over the past 15 000 years. Antarct. Sci. 33, 103–115. https://doi.org/10.1017/S0954102020000541.

Charton, J., Schimmelpfennig, I., Jomelli, V., Delpech, G., Blard, P.H., Braucher, R., Verfaillie, D., Favier, V., Rinterknecht, V., Goosse, H., Crosta, X., Chassiot, L., Martin, L., Guillaume, D., Legentil, C., 2022. New cosmogenic nuclide constraints on late glacial and Holocene glacier fluctuations in the sub-Antarctic Indian ocean (Kerguelen islands, 49°S). Quat. Sci. Rev. 283 https://doi.org/10.1016/j.quascirev.2022.107461.

Chau, J.H., Born, C., McGeoch, M.A., Bergstrom, D., Shaw, J., Terauds, A., Mairal, M., Le Roux, J.J., Jansen van Vuuren, B., 2019. The influence of landscape, climate and history on spatial genetic patterns in keystone plants (Azorella) on sub-Antarctic islands. Mol. Ecol. 28, 3291–3305. https://doi.org/10.1111/mec.15147.

Chevallier, L., 1986. Tectonics of Marion and Prince Edward volcanoes (Indian Ocean): result of regional control and edifice dynamics. Tectonophysics 124, 155–175. https://doi.org/10.1016/0040-1951(86)90143-5.

Clark, P.U., Dyke, A.S., Shakun, J.D., Carlson, A.E., Clark, J., Wohlfarth, B., Mitrovica, J. X., Hostetler, S.W., McCabe, A.M., 2009. The Last Glacial Maximum. Science (80-325, 710–714. https://doi.org/10.1126/science.1172873.

Crosta, X., Sturm, A., Armand, L., Pichon, J.J., 2004. Late Quaternary sea ice history in the Indian sector of the Southern Ocean as recorded by diatom assemblages. Mar. Micropaleontol. 50, 209–223. https://doi.org/10.1016/S0377-8398(03)00072-0.

Darvill, C.M., Bentley, M.J., Stokes, C.R., Shulmeister, J., 2016. The timing and cause of glacial advances in the southern mid-latitudes during the last glacial cycle based on a synthesis of exposure ages from Patagonia and New Zealand. Quat. Sci. Rev. 149, 200–214. https://doi.org/10.1016/j.quascirev.2016.07.024.

De Boer, A.M., Graham, R.M., Thomas, M.D., Kohfeld, K.E., 2013. The control of the Southern Hemisphere Westerlies on the position of the subtropical front. J. Geophys. Res. Ocean. 118, 5669–5675. https://doi.org/10.1002/jgrc.20407.

De Deckker, P., Arnold, L.J., van der Kaars, S., Bayon, G., Stuut, J.B.W., Perner, K., Lopes dos Santos, R., Uemura, R., Demuro, M., 2019. Marine Isotope Stage 4 in Australasia: a full glacial culminating 65,000 years ago – global connections and implications for human dispersal. Quat. Sci. Rev. 204, 187–207. https://doi.org/10.1016/j.quascirev.2018.11.017.

Denton, G.H., Putnam, A.E., Russell, J.L., Barrell, D.J.A., Schaefer, J.M., Kaplan, M.R., Strand, P.D., 2021. The Zealandia Switch: ice age climate shifts viewed from Southern Hemisphere moraines. Quat. Sci. Rev. 257, 106771 https://doi.org/10.1016/j.quascirev.2020.106771.

Di Nicola, L., Schnabel, C., Wilcken, K.M., Gméling, K., 2009. Determination of chlorine concentrations in whole rock: Comparison between prompt-gamma activation and isotope-dilution AMS analysis. Quat. Geochronol. 4, 501–507. https://doi.org/10.1016/j.quageo.2009.08.001.

Doughty, A.M., Schaefer, J.M., Putnam, A.E., Denton, G.H., Kaplan, M.R., Barrell, D.J.A., Andersen, B.G., Kelley, S.E., Finkel, R.C., Schwartz, R., 2015. Mismatch of glacier extent and summer insolation in Southern Hemisphere mid-latitudes. Geology 43, 407–410. https://doi.org/10.1130/G36477.1.

Dunai, T., 2010. Cosmogenic Nuclides: Principles, Concepts and Applications in Earth Surface Sciences. Cambridge University Press, New York. https://doi.org/10.1007/s13398-014-0173-7.2.

Eaves, S.R., Mackintosh, A.N., Winckler, G., Schaefer, J.M., Alloway, B.V., Townsend, D. B., 2016. A cosmogenic 3He chronology of late Quaternary glacier fluctuations in North Island, New Zealand (39°S). Quat. Sci. Rev. 132, 40–56. https://doi.org/10.1016/j.quascirev.2015.11.004.

Eaves, S.R., Mackintosh, A.N., Anderson, B.M., 2019. Climate amelioration during the Last Glacial Maximum recorded by a sensitive mountain glacier in New Zealand. Geology 47, 299–302. https://doi.org/10.1130/G45543.1.

EPICA, 2006. One-to-one coupling of glacial climate variability in Greenland and Antarctica. Nature 444, 195–198. https://doi.org/10.1038/nature05301.

García, J.L., Hein, A.S., Binnie, S.A., Gómez, G.A., González, M.A., Dunai, T.J., 2018. The MIS 3 maximum of the Torres del Paine and Última Esperanza ice lobes in Patagonia and the pacing of southern mountain glaciation. Quat. Sci. Rev. 185, 9–26. https://doi.org/10.1016/j.quascirev.2018.01.013.

Gersonde, R., Crosta, X., Abelmann, A., Armand, L., 2005. Sea-surface temperature and sea ice distribution of the Southern Ocean at the EPILOG Last Glacial Maximum - a circum-Antarctic view based on siliceous microfossil records. Quat. Sci. Rev. 24, 869–896. https://doi.org/10.1016/j.quascirev.2004.07.015.

Graham, A.G.C.C., Kuhn, G., Meisel, O., Hillenbrand, C.-D.D., Hodgson, D.A., Ehrmann, W., Wacker, L., Wintersteller, P., Dos Santos Ferreira, C., Römer, M., White, D., Bohrmann, G., 2017. Major advance of South Georgia glaciers during the Antarctic Cold Reversal following extensive sub-Antarctic glaciation. Nat. Commun. 8, 14798 https://doi.org/10.1038/ncomms14798.

Hall, K., 1978. Quaternary Glacial Geology of Marion Island. Bloemfontein : U.O.F.S.

Hall, K., Meiklejohn, I., Bumby, A., 2011. Marion Island volcanism and glaciation. Antarct. Sci. 23, 155–163. https://doi.org/10.1017/S0954102010000878.

Haussmann, N., Aldahan, A., Boelhouwers, J., Possnert, G., 2010. 10Be application to soil development on Marion Island, southern Indian Ocean. Nucl. Instruments Methods Phys. Res. Sect. B Beam Interact. with Mater. Atoms 268, 1058–1061. https://doi.org/10.1016/j.nimb.2009.10.097.

Hedding, D.W., 2008. Spatial inventory of landforms in the recently exposed central highland of Sub-Antarctic Marion Island. South African Geogr. J 90, 11–21. https://doi.org/10.1080/03736245.2008.9725307.

Hedding, D.W., Greve, M., 2018. Decreases in precipitation on sub-Antarctic Marion Island: implications for ecological and geomorphological processes'. Weather 73, 203. https://doi.org/10.1002/wea.3245.

Hedding, D.W., Brook, M.S., Winkler, S., 2018. Old landscapes, new eyes: revisiting geomorphological research in the Southern Alps of New Zealand. N. Z. Geog. 74, 109–112. https://doi.org/10.1111/nzg.12189.

Hodgson, D.A., Graham, A.G.C., Griffiths, H.J., Roberts, S.J., Ó Cofaigh, C., Bentley, M.J., Evans, D.J.A., 2014a. Glacial history of sub-Antarctic South Georgia based on the submarine geomorphology of its fjords. Quat. Sci. Rev. 89, 129–147. https://doi.org/10.1016/j.quascirev.2013.12.005.

Hodgson, D.A., Graham, A.G.C., Roberts, S.J., Bentley, M.J., Ó Cofaigh, C., Verleyen, E., Vyverman, W., Jomelli, V., Favier, V., Brunstein, D., Verfaillie, D., Colhoun, E.A., Saunders, K.M., Selkirk, P.M., Mackintosh, A., Hedding, D.W., Nel, W., Hall, K., Mcglone, M., Van Der Putten, N., Dickens, W.A., Smith, J.A., 2014b. Terrestrial and submarine evidence for the extent and timing of the Last Glacial Maximum and the onset of deglaciation on the maritime- Antarctic and sub-Antarctic islands. Quat. Sci. Rev. 100, 137–158. https://doi.org/10.1016/j.quascirev.2013.12.001.

Ivy-Ochs, S., Kober, F., 2008. Surface exposure dating with cosmogenic nuclides. Quat. Sci. J. (Eiszeitalter und Gegenwart) 57, 179–209. https://doi.org/10.3285/eg.57.1-2.7.

Jomelli, V., Mokadem, F., Schimmelpfennig, I., Chapron, E., Rinterknecht, V., Favier, V., Verfaillie, D., Brunstein, D., Legentil, C., Michel, E., Swingedouw, D., Jaouen, A., Aumaitre, G., Bourlès, D.L., Keddadouche, K., 2017. Sub-Antarctic glacier extensions in the Kerguelen region (49°S, Indian Ocean) over the past 24,000 years constrained by36Cl moraine dating. Quat. Sci. Rev. 162, 128–144. https://doi.org/10.1016/j.quascirev.2017.03.010.

Jomelli, V., Schimmelpfennig, I., Favier, V., Mokadem, F., Landais, A., Rinterknecht, V., Brunstein, D., Verfaillie, D., Legentil, C., Aumaitre, G., Bourlès, D.L., Keddadouche, K., 2018. Glacier extent in sub-Antarctic Kerguelen archipelago from MIS 3 period: evidence from36Cl dating. Quat. Sci. Rev. 183, 110–123. https://doi.org/10.1016/j.quascirev.2018.01.008.

Jouzel, J., Masson-Delmotte, V., Cattani, O., Dreyfus, G., Falourd, S., Hoffmann, G., Minster, B., Nouet, J., Barnola, J.M., Chappellaz, J., Fischer, H., Gallet, J.C., Johnsen, S., Leuenberger, M., Loulergue, L., Luethi, D., Oerter, H., Parrenin, F., Raisbeck, G., Raynaud, D., Schilt, A., Schwander, J., Selmo, E., Souchez, R., Spahni, R., Stauffer, B., Steffensen, J.P., Stenni, B., Stocker, T.F., Tison, J.L., Werner, M., Wolff, E.W., 2007. Orbital and Millennial Antarctic climate variability over the past 800,000 Years. Science (80) 317, 793–796. https://doi.org/10.1126/science.1141038.

Knight, J., Shulmeister, J., Petherick, L., 2021. Introduction to the SHeMax Thematic Set and Prospects for LGM Research in the Southern Hemisphere 1–4. https://doi.org/10.1017/qua.2021.39.

Köse, O., Sarıkaya, M.A., Çiner, A., Candaş, A., Yıldırım, C., Wilcken, K.M., 2022. Reconstruction of last glacial maximum glaciers and palaeoclimate in the central Taurus range, Mt. Karanfil, of the eastern mediterranean. Quat. Sci. Rev. 291 https://doi.org/10.1016/j.quascirev.2022.107656.

Lamont, T., Toolsee, T., 2022. Spatial and seasonal variations of the island mass effect at the sub-antarctic prince edward islands archipelago. Remote Sens 14. https://doi.org/10.3390/rs14092140.

Le Roex, A.P.P., Chevallier, L., Verwoerd, W.J.J., Barends, R., 2012. Petrology and geochemistry of Marion and Prince Edward islands, Southern Ocean: magma chamber processes and source region characteristics. J. Volcanol. Geotherm. Res. 223–224, 11–28. https://doi.org/10.1016/j.jvolgeores.2012.01.009.

Le Roux, P.C., 2008. Climate and climate change. In: Chown, S.L., Froneman, P.W. (Eds.), The Prince Edward Islands: Land-Sea Interactions in a Changing Ecosystem. SUN PRESS, Stellenbosch, pp. 39–64. https://doi.org/10.18820/9781928314219/03.

Lenaerts, J.T.M., Van Den Broeke, M.R., Van Wessem, J.M., Van De Berg, W.J., Van Meijgaard, E., Van Ulft, L.H., Schaefer, M., 2014. Extreme precipitation and climate gradients in patagonia revealed by high-resolution regional atmospheric climate modeling. J. Clim. 27, 4607–4621. https://doi.org/10.1175/JCLI-D-13-00579.1.

Lešić, N.M., Streuff, K.T., Bohrmann, G., Kuhn, G., 2022. Glacimarine sediments from outer Drygalski trough, sub-antarctic south Georgia – evidence for extensive glaciation during the last glacial maximum. Quat. Sci. Rev. 292 https://doi.org/10.1016/j.quascirev.2022.107657.

Li, Y.K., 2018. Determining topographic shielding from digital elevation models for cosmogenic nuclide analysis: a GIS model for discrete sample sites. J. Mt. Sci. 15, 939–947. https://doi.org/10.1007/s11629-018-4895-4.

Lifton, N., Sato, T., Dunai, T.J., 2014. Scaling in situ cosmogenic nuclide production rates using analytical approximations to atmospheric cosmic-ray fluxes. Earth Planet Sci. Lett. 386, 149–160. https://doi.org/10.1016/j.epsl.2013.10.052.

Lutjeharms, J., Ansorge, I.J., 2008. Oceanographic setting of the prince edward islands. In: Chown, S.L., Froneman, P.W. (Eds.), Prince Edward Islands: Land-Sea Interactions in a Changing Ecosystem. SUN PReSS, Stellenbosch, pp. 17–38. https://doi.org/10.18820/9781928314219/02.

Mackintosh, A.N., Barrows, T.T., Colhoun, E.A., Fifield, L.K., 2006. Exposure dating and glacial reconstruction at Mt. Field, Tasmania, Australia, identifies MIS 3 and MIS 2 glacial advances and climatic variability. J. Quat. Sci. 21, 363–376. https://doi.org/10.1002/jqs.989.

Marrero, S.M., 2012. Calibration of Cosmogenic Chlorine-36. New Mexico Insitute fof Mining and Technology.

Marrero, S.M., Phillips, F.M., Borchers, B., Lifton, N., Aumer, R., Balco, G., 2016a. Cosmogenic nuclide systematics and the CRONUScalc program. Quat. Geochronol. 31, 160–187. https://doi.org/10.1016/j.quageo.2015.09.005.

Marrero, S.M., Phillips, F.M., Caffee, M.W., Gosse, J.C., 2016b. CRONUS-Earth cosmogenic 36Cl calibration. Quat. Geochronol. 31, 199–219. https://doi.org/10.1016/j.quageo.2015.10.002.

Masarik, J., Wieler, R., 2003. Production rates of cosmogenic nuclides in boulders. Earth Planet Sci. Lett. 216, 201–208. https://doi.org/10.1016/S0012-821X(03)00476-X.

McDougall, I., Verwoerd, W.J., Chevallier, L., 2001. K–Ar geochronology of marion island. Southern Ocean. Geol. Mag. 138, 1–17.

Mélice, J.-L., Lutjeharms, J., Rouault, M., Ansorge, I., 2003. Sea-surface temperatures at the sub-Antarctic islands Marion and Gough during the past 50 years. South Afr. J. Sci. 99, 363–366.

Miller, K.G., Browning, J.V., John Schmelz, W., Kopp, R.E., Mountain, G.S., Wright, J.D., 2020. Cenozoic sea-level and cryospheric evolution from deep-sea geochemical and continental margin records. Sci. Adv. 6 https://doi.org/10.1126/sciadv.aaz1346.

Momberg, M., Hedding, D.W., Luoto, M., Roux, P.C., 2021. Exposing wind stress as a driver of fine-scale variation in plant communities. J. Ecol. 109, 2121–2136. https://doi.org/10.1111/1365-2745.13625.

Nel, W., Boelhouwers, J.C., Borg, C.-J., Cotrina, J.H., Hansen, C.D., Haussmann, N.S., Hedding, D.W., Meiklejohn, K.I., Nguna, A.A., Rudolph, E.M., Sinuka, S.S., Sumner, P.D., 2021. Earth science research on Marion Island (1996–2020): a synthesis and new findings. S. Afr. Geogr. J. 103, 22–42. https://doi.org/10.1080/03736245.2020.1786445.

Nel, W., Hedding, D.W., Rudolph, E.M., 2023. The sub-Antarctic islands are increasingly warming in the 21st Century. Antarct. Sci. (2) 35,, 124–126.

Parrenin, F., Masson-Delmotte, V., Köhler, P., Raynaud, D., Paillard, D., Schwander, J., Barbante, C., Landais, A., Wegner, A., Jouzel, J., 2013. Synchronous change of atmospheric CO2 and Antarctic temperature during the last deglacial warming. Science (80) 339, 1060–1063. https://doi.org/10.1126/science.1226368.

Petherick, L.M., Knight, J., Shulmeister, J., Bostock, H., Lorrey, A., Fitchett, J., Eaves, S., Vandergoes, M.J., Barrows, T.T., Barrell, D.J.A., Eze, P.N., Hesse, P., Jara, I.A., Mills, S., Newnham, R., Pedro, J., Ryan, M., Saunders, K.M., White, D., Rojas, M., Turney, C., 2022. An extended last glacial maximum in the Southern Hemisphere: a contribution to the SHeMax project. Earth Sci. Rev. 231, 104090 https://doi.org/10.1016/j.earscirev.2022.104090.

Putnam, A.E., Denton, G.H., Schaefer, J.M., Barrell, D.J.A., Andersen, B.G., Finkel, R.C., Schwartz, R., Doughty, A.M., Kaplan, M.R., Schlüchter, C., 2010. Glacier advance in southern middle-latitudes during the Antarctic Cold Reversal. Nat. Geosci. 3, 700–704. https://doi.org/10.1038/ngeo962.

Putnam, A.E., Schaefer, J.M., Denton, G.H., Barrell, D.J.A., Birkel, S.D., Andersen, B.G., Kaplan, M.R., Finkel, R.C., Schwartz, R., Doughty, A.M., 2013. The last glacial maximum at 44°S documented by a 10Be moraine chronology at lake ohau, southern Alps of New Zealand. Quat. Sci. Rev. 62, 114–141. https://doi.org/10.1016/j.quascirev.2012.10.034.

Railsback, L.B., Gibbard, P.L., Head, M.J., Voarintsoa, N.R.G., Toucanne, S., 2015. An optimized scheme of lettered marine isotope substages for the last 1.0 million years, and the climatostratigraphic nature of isotope stages and substages. Quat. Sci. Rev. 111, 94–106. https://doi.org/10.1016/j.quascirev.2015.01.012.

Rainsley, E., Turney, C.S.M., Golledge, N.R., Wilmshurst, J.M., McGlone, M.S., Hogg, A. G., Li, B., Thomas, Z.A., Roberts, R., Jones, R.T., Palmer, J.G., Flett, V., De Wet, G., Hutchinson, D.K., Lipson, M.J., Fenwick, P., Hines, B., Binetti, U., Fogwill, C.J., 2019. Pleistocene glacial history of the New Zealand subantarctic islands. Clim. Past 15, 423–448. https://doi.org/10.5194/cp-15-423-2019.

Rouault, M., Mélice, J.L., Reason, C.J.C., Lutjeharms, J.R.E., 2005. Climate variability at marion island, Southern Ocean, since 1960. J. Geophys. Res. C Oceans 110, 1–9. https://doi.org/10.1029/2004JC002492.

Rudolph, E.M., Hedding, D.W., Fabel, D., Hodgson, D.A., Gheorghiu, D.M., Shanks, R., Nel, W., 2020. Early glacial maximum and deglaciation at sub-Antarctic Marion Island from cosmogenic 36Cl exposure dating. Quat. Sci. Rev. 231, 106208 https://doi.org/10.1016/j.quascirev.2020.106208.

Rudolph, E.M., Hedding, D.W., Nel, W., 2021a. The glacial geomorphology of sub-Antarctic Marion Island. J. Maps 17, 313–324. https://doi.org/10.1080/17445647.2021.1931970.

Rudolph, E.M., Hedding, D.W., Nel, W., 2021b. The surface geology of the Prince Edward Islands: refined spatial data and call for geoconservation. S. Afr. J. Geol. 124, 627–638. https://doi.org/10.25131/sajg.124.0014.

Rudolph, E.M., Hedding, D.W., Nel, W., 2022a. A spatial model of Marion Island's palaeo-ice extent. Antarct. Sci. 1–9 https://doi.org/10.1017/S0954102022000293.

Rudolph, E.M., Hedding, D.W., de Bruyn, P.J.N., Nel, W., 2022b. An open access geospatial database for the sub-Antarctic Prince Edward Islands. South Afr. J. Sci. 118 (9/10) https://doi.org/10.17159/sajs.2022/12302. Art. #12302.

Rudolph, E.M., Hedding, D., Hodgson, D., Fabel, D., Gheorghiu, D., Shanks, R., Nel, W., 2023. Marion Island 36Cl Exposure Ages from MIS2/3: the CRONUScalc Input File. https://doi.org/10.17632/wkwm6kg9hc.1.

Schaefer, J.M., Putnam, A.E., Denton, G.H., Kaplan, M.R., Birkel, S., Doughty, A.M., Kelley, S., Barrell, D.J.A., Finkel, R.C., Winckler, G., Anderson, R.F., Ninneman, U.S., Barker, S., Schwartz, R., Andersen, B.G., Schluechter, C., 2015. The southern glacial maximum 65,000 years ago and its unfinished termination. Quat. Sci. Rev. 114, 52–60. https://doi.org/10.1016/j.quascirev.2015.02.009.

Schulze, B., 1971. Climate. In: Winterbottom, J.M., Dyer, R. (Eds.), Marion and Prince Edward Islands: Report on the South African Biological and Geological Research Expedition 1965-19661. A.A. Balkema, Cape Town.

Shulmeister, J., Thackray, G.D., Rittenour, T.M., Fink, D., Patton, N.R., 2019. The timing and nature of the last glacial cycle in New Zealand. Quat. Sci. Rev. 206, 1–20. https://doi.org/10.1016/j.quascirev.2018.12.020.

Sime, L.C., Kohfeld, K.E., Le Quéré, C., Wolff, E.W., de Boer, A.M., Graham, R.M., Bopp, L., 2013. Southern Hemisphere westerly wind changes during the Last Glacial Maximum: model-data comparison. Quat. Sci. Rev. 64, 104–120. https://doi.org/10.1016/J.QUASCIREV.2012.12.008.

Sime, L.C., Hodgson, D.A., Bracegirdle, T.J., Allen, C., Perren, B., Roberts, S., De Boer, A. M., 2016. Sea ice led to poleward-shifted winds at the Last Glacial Maximum: the

influence of state dependency on CMIP5 and PMIP3 models. Clim. Past 12, 2241–2253. https://doi.org/10.5194/cp-12-2241-2016.

Smith, V.R., 2002. Climate change in the sub-Antarctic: an illustration from Marion Island. Clim. Change 52, 345–357.

Smith, V.R., Steenkamp, M., 1990. Climatic change and its ecological implications at a subantarctic island. Oecologia 85, 14–24.

Solomina, O.N., Bradley, R.S., Hodgson, D.A., Ivy-Ochs, S., Jomelli, V., Mackintosh, A.N., Nesje, A., Owen, L.A., Wanner, H., Wiles, G.C., Young, N.E., 2015. Holocene glacier fluctuations. Quat. Sci. Rev. 111, 9–34. https://doi.org/10.1016/j.quascirev.2014.11.018.

Solomina, O.N., Bradley, R.S., Jomelli, V., Geirsdottir, A., Kaufman, D.S., Koch, J., McKay, N.P., Masiokas, M., Miller, G., Nesje, A., Nicolussi, K., Owen, L.A., Putnam, A.E., Wanner, H., Wiles, G., Yang, B., 2016. Glacier fluctuations during the past 2000 years. Quat. Sci. Rev. 149, 61–90. https://doi.org/10.1016/j.quascirev.2016.04.008.

Sumner, P.D., Meiklejohn, K.I., 2004. On the development of autochthonous blockfields in the grey basalts of sub-Antarctic Marion Island. Polar Geogr. 28, 120–132. https://doi.org/10.1080/789610121.

Sumner, P.D., Nel, W., Holness, S., Boelhouwers, J.C., 2002. Rock weathering characteristics as relative-age indicators for glacial and post-glacial landforms on Marion Island. S. Afr. Geogr. J. 84, 153–157.

Toggweiler, J.R., Russell, J., 2008. Ocean circulation in a warming climate. Nature 451, 286–288. https://doi.org/10.1038/nature06590.

Toolsee, T., Lamont, T., 2022. Long-term trends and interannual variability of wind forcing, surface circulation, and temperature around the sub-antarctic prince edward islands. Remote Sens 14, 1–28. https://doi.org/10.3390/rs14061318.

Verfaillie, D., Charton, J., Schimmelpfennig, I., Stroebele, Z., Jomelli, V., Bétard, F., Favier, V., Cavero, J., Berthier, E., Goosse, H., Rinterknecht, V., Legentil, C., Charrassin, R., Aumaître, G., Bourlès, DiL., Keddadouche, K., 2021. Evolution of the Cook Ice Cap (Kerguelen Islands) between the last centuries and 2100 ce based on cosmogenic dating and glacio-climatic modelling. Antarct. Sci. 33, 301–317. https://doi.org/10.1017/S0954102021000080.

Verwoerd, W.J., 1971. Geology. In: Van Zinderen Bakker Sr, E., Winterbottom, J.M., Dyer, R. (Eds.), Marion and Prince Edward Islands: Report on the South African Biological and Geological Research Expedition 1965-1966. A.A. Balkema, Cape Town, pp. 40–62.

White, D.A., Bennike, O., Melles, M., Berg, S., Binnie, S.A., 2018. Was South Georgia covered by an ice cap during the last glacial maximum? In: Siegert, M., Jamieson, S., White, D. (Eds.), Exploration of Subsurface Antarctica: Uncovering Past Changes and Modern Processes. Geological Society, Special Publications, London, pp. 49–59. https://doi.org/10.1144/SP461.4.